Available online at www.sciencedirect.com

ScienceDirect

Geochimica et Cosmochimica Acta 223 (2018) 462–492

Geochimica et Cosmochimica Acta

www.elsevier.com/locate/gca

Petrography of the carbonaceous, diamond-bearing stone "Hypatia" from southwest Egypt: A contribution to the debate on its origin

Georgy A. Belyanin[a], Jan D. Kramers[a,*], Marco A.G. Andreoli[b], Francesco Greco[a,c], Arnold Gucsik[a,d,e], Tebogo V. Makhubela[a], Wojciech J. Przybylowicz[f,g], Michael Wiedenbeck[h]

[a] *Department of Geology, University of Johannesburg, PO Box 524, Auckland Park 2006, South Africa*
[b] *School of Geosciences, University of the Witwatersrand, PO Box 3, Wits 2050, South Africa*
[c] *Dipartimento di Scienze Biologiche, Geologiche ed Ambientali, Università di Bologna, Via Zamboni 67, 40126 Bologna, Italy*
[d] *Department of Nonlinear and Laser Optics, Wigner Research Institute for Physics, Hungarian Academy of Sciences, Konkoly-Thege Miklós út 29-33, Budapest H-1121, Hungary*
[e] *Department of Mineralogy and Geology, Cosmochemistry Research Group, University of Debrecen, Egyetem tér 1., H-4032, Hungary*
[f] *iThemba Labs, National Research Foundation, P.O. Box 722, Somerset West 7129, South Africa*
[g] *AGH University of Science and Technology, Faculty of Physics & Applied Computer Science, 30-059 Kraków, Poland*
[h] *Deutsches GeoForschungsZentrum GFZ, D14473 Potsdam, Germany*

Received 15 June 2017; accepted in revised form 20 December 2017; Available online 28 December 2017

Abstract

The stone named "Hypatia" found in the Libyan Desert Glass area of southwest Egypt is carbon-dominated and rich in microdiamonds. Previous noble gas and nitrogen isotope studies suggest an extraterrestrial origin. We report on a reconnaissance study of the carbonaceous matrix of this stone and the phases enclosed in it. This focused on areas not affected by numerous transecting fractures mostly filled with secondary minerals. The work employed scanning electron microscopy (SEM) with energy-dispersive (EDS) and wavelength-dispersive (WDS) electron microprobe (EMPA) analysis, Proton Induced X-ray Emission (PIXE) spectrometry and micro-Raman spectroscopy. We found that carbonaceous matrices of two types occur irregularly intermingled on the 50–500 µm scale: Matrix-1, consisting of almost pure carbonaceous matter, and Matrix-2, containing Fe, Ni, P and S at abundances analyzable by microprobe. Matrix-2 contains the following phases as inclusions: (i) (Fe,Ni) sulphide occurring in cloud-like concentrations of sub-µm grains, in domains of the matrix that are enriched in Fe and S. These domains have (Fe + Ni)/S (atomic) = 1.51 ± 0.24 and Ni/Fe = 0.086 ± 0.061 (both 1SD); (ii) grains up to ~5 µm in size of moissanite (SiC); (iii) Ni-phosphide compound grains up to 60 µm across that appear cryptocrystalline or amorphous and have (Ni + Fe)/P (atomic) = 5.6. ± 1.7 and Ni/Fe = 74 ± 29 (both 1SD), where both these ratios are much higher than any known Ni-phosphide minerals; (iv) rare grains (observed only once) of graphite, metallic Al, Fe and Ag, and a phase consisting of Ag, P and I. In Matrix-2, Raman spectroscopy shows a prominent narrow diamond band at 1340 cm^{-1}. In Matrix-1 the D and G bands of disordered carbon are dominant, but a minor diamond band is ubiquitous, accounting for the uniform hardness of the material. The D and G bands have average full width at half maximum (FWHM) values of 295 ± 19 and 115 ± 19 cm^{-1}, respectively, and the D/G intensity ratio is 0.75 ± 0.09 (both 1SD). These values are similar to those of the most primitive solar system carbonaceous matter. The diamond phase is considered to be a product of shock. The (Fe, Ni) sulphide phase is probably pyrrhotite and a shock origin is likewise proposed for it. Moissanite is

---

* Corresponding author.
E-mail address: jkramers@uj.ac.za (J.D. Kramers).

https://doi.org/10.1016/j.gca.2017.12.020

frequently associated with the Ni-phosphide phase, and a presolar origin for both is suggested. The lack of recrystallization of the Ni-phosphide phase suggests that the Hypatia stone did not experience long-lasting thermal metamorphism, in accord with the Raman D-G band characteristics.

A lack of silicate matter sets the stone apart from interplanetary dust particles and known cometary material. This, along with the dual intermingled matrices internal to it, could indicate a high degree of heterogeneity in the early solar nebula.

Keywords: Extraterrestrial carbonaceous matter; Silicon carbide; Nickel phosphide; Shock metamorphism; Early solar nebula heterogeneity

1. INTRODUCTION

A carbon-rich, microdiamond-bearing stone 30 grams in mass and of dimensions 3.5 × 3.2 × 2.1 cm was found in 1996 by Aly A. Barakat in the Libyan Desert Glass (LDG) area in southwestern Egypt. Barakat (2012) describes it as extremely hard yet very brittle and heavily fractured, and showing a curious pitch-like lustre beneath the coating of desert varnish. Its enigmatic appearance and physical properties motivated recent multidisciplinary studies (Kramers et al., 2013, who named it "Hypatia"; Andreoli et al., 2015; Avice et al., 2015).

Original suspicions that the stone might be an unusual variety of carbonado diamond, a type of polycrystalline diamond found in Brazil and the Central African Republic (e.g. Trueb and de Wys, 1969; De et al., 1998; Haggerty, 2014) were set aside by $\delta^{13}C$ values of −0.2‰ and −1.1‰ (Kramers et al., 2013) in contrast to the values between −30‰ and −12‰ obtained on carbonados (Shelkov et al., 1997; De et al., 2001). Further, Kramers et al. (2013) and Avice et al. (2015) reported $^{40}Ar/^{36}Ar$ ratios (~39 and ~0.5, respectively) far lower than the lowest present-day terrestrial value, which is the atmospheric ratio, 298.56 ± 0.31 (Lee et al., 2006). Avice et al. (2015) also found He, Ne and Xe with isotopic compositions distinctly different from terrestrial values, but very similar to those of the "Q" noble gas component, which is dominant in chondritic meteorites, where it is hosted in insoluble organic matter (IOM; Lewis et al., 1975; Ozima et al., 1998; Busemann et al., 2000; Ott, 2002). From cosmogenic ^{21}Ne data, Avice et al. (2015) further find that Hypatia must have been part of a bolide at least several m in diameter and if the body was much larger, the stone must have come from the outermost few m.

Nitrogen isotope data from Hypatia (Avice et al., 2015) present a bimodal picture, with low temperature releases yielding $^{15}N/^{14}N$ ratios of ~0.00376 ($\delta^{15}N \sim +20‰$) and the dominant release at high temperatures ~0.00327 ($\delta^{15}N \sim -110‰$). While $\delta^{15}N$ values up to +20‰ and +50‰ have been measured in Phanerozoic and Archean shales, respectively (Thomazo and Papineau, 2013), values below −10‰ are very rare, and values below −40‰ have never been found in any terrestrial (crustal or mantle-derived) material (Cartigny and Marty, 2013). These nitrogen isotope data allow comparisons with various types of extraterrestrial objects. Primitive carbonaceous chondrites have $^{15}N/^{14}N$ ratios higher than 0.0036 ($\delta^{15}N > -20$) (Füri and Marty, 2015). Avice et al. (2015) noted similarities of the light Hypatia values with diamonds in ureilites (Rai et al., 2003a) and graphite nodules in iron meteorites (Grady and Wright, 2003). Among primitive, carbon-rich objects, a very wide range of $^{15}N/^{14}N$ ratios has been found: from 0.0031 to 0.0072 ($\delta^{15}N$: −150‰ to +970‰), by high resolution spectrometry, for comets (Jewitt et al., 1997; Arpigny et al., 2003; Bockelée-Morvan et al., 2008) and from 0.0033 to 0.0055 ($\delta^{15}N$: −97‰ to +505‰), by mass spectrometry, in bulk primitive interplanetary dust particles (IDP's) and in comet 81P/Wild dust (Floss et al., 2006; McKeegan et al., 2006). The Hypatia data fall in the lightest part of this range, which as a whole is strongly fractionated towards ^{15}N relative to the best estimate for the bulk solar nebula (0.00227; $\delta^{15}N$: −379‰, Marty et al., 2010, 2011; Füri and Marty, 2015).

In Hypatia's carbonaceous matrix, X-ray diffraction (XRD), Raman spectroscopy and transmission electron microscopy (TEM) have revealed the presence of diamond (Kramers et al., 2013; Avice et al., 2015). TEM has shown that this diamond occurs as grains between 50 nm and 2 μm in size (Kramers et al., 2013; Avice et al., 2015). A comparison of TEM images with those of diamonds from the Popigai impact structure (Koeberl et al., 1997) suggests that the diamond was probably formed as a result of shock (Kramers et al., 2013). A widening of the X-ray diffraction patterns, the presence of the hexagonal diamond polymorph lonsdaleite, and distinct deformation bands visible by TEM also point to a shock-related origin (Avice et al., 2015). In Raman spectroscopy, the presence of disordered carbonaceous matter is revealed by both D and G bands as well as a high fluorescence background (Kramers et al., 2013).

In a microchemical study using Proton Induced X-ray Emission (PIXE) analysis, Andreoli et al. (2015) found extraordinary heterogeneity on the 100 μm-scale, with, for instance, regions showing up to 4‰ Ir and up to 0.6‰ Os and variable element distributions that do not show any relationship to established cosmochemical groupings.

The stone, when discovered, was larger by orders of magnitude than any carbon-dominated object of extraterrestrial origin found on Earth, with the exception of graphite-rich nodules in the Canyon Diablo meteorite (Vdovykin, 1973). Kramers et al. (2013) suggested that it is a remnant of a cometary nucleus fragment and suggested that it may have originated from a bolide which broke up and exploded in the atmosphere causing the formation of the LDG. This suggestion was dismissed by Reimold and Koeberl (2014), who state categorically: "There is no connection between the diamond-bearing rock fragment and the LDG except that they occur in the same region".

Avice et al. (2015) noted that the Hypatia stone is unlike any solar system object ever studied in the laboratory. As the $\delta^{15}N$ values measured in Hypatia are much lower than those mostly determined for comets (see above) they do not favour the hypothesis of a cometary origin, although they consider that it cannot be excluded completely on the basis of available data. The debate on the origin of the Hypatia stone is thus clearly not settled.

During the seventeen years that elapsed between the discovery of the stone and the first publication of indications for an extraterrestrial origin (Kramers et al., 2013), a significant part of the material was dispersed over various unknown locations on Planet Earth. At the time of writing, the whereabouts of less than 4 g of Hypatia's matter are known to us. This has thus far prevented classification of Hypatia as a meteorite, as the Meteoritical Society stipulates for this a repository mass at least 20% of the total discovery mass of the object. This circumstance has however not brought research on Hypatia to a halt. Within its carbonaceous matrix, the stone contains a variety of mineral inclusions (Kramers et al., 2013). Apart from the diamond content, no mineralogical data have yet been published that could shed light on the stone's origin or the physical conditions of its formation. In order to fill this knowledge gap, we have carried out mineralogical and microchemical assays using scanning electron microscopy, electron microprobe, PIXE and micro-Raman analysis on two polished sections. We have studied both the carbonaceous matrix and mineral inclusions, report the results in a textural context and compare them with carbonados and (in view of our hypothesis that the Hypatia stone is of extraterrestrial origin) various types of meteoritic matter, as well as IDP's and cometary dust. This study is thus aimed at contributing to the debate on the origin of this enigmatic object.

2. SAMPLES, PREPARATION AND ANALYTICAL METHODS

A small (~3 × 8 × 4 mm) piece of the stone was prised off a sample aliquot in the custody of one of us (M.A.G.A.), mounted in epoxy resin and polished by M. Reback at iThemba Labs, Johannesburg, producing Reback/A (referred to below as sample A and identical to Hyp-3 of Kramers et al., 2013). This was polished further at the University of Johannesburg (UJ) using a Struers PdM-Force-20 machine rotating at 600 rpm and Struers MD Piano 120 diamond disk. Further polishing was done using Struers MD polishing cloths at 160–180 rpm with application of DP-Stick P (containing exclusively polycrystalline diamonds), starting with 3 μm for 1–2 h, followed by 1 and then 1/4 μm for many hours. In spite of the extreme hardness and brittle nature of the sample, a flatness suitable for micro- scanning electron microscope, electron microprobe and micro-Raman work, was achieved in small (~50–200 μm) localised areas. A broken-out fragment (~1 × 3 × 1 mm, see Fig. 1) was separately mounted and polished. This was used for PIXE analyses (Andreoli et al., 2015) and was then subsequently sent to the Helmholtz Zentrum Potsdam (GFZ) in Germany. There it was extracted from its mount and repolished using a Franz Amann ESK35 diamond polishing instrument. During this polishing, which lasted a few seconds, the sample was held in a metal clamp and was ground flat using a diamond sintered wheel made of a Zn-Co-Cu alloy which rotated at 5000 rpm. Subsequent white light interferometry documented that sample roughness over large areas was less than 1 μm, patches where material had been plucked out were also present. Subsequent to polishing, the GFZ piece of Hypatia was cast in epoxy. This is referred to below as sample B. At neither institute and at no stage were polishing media containing moissanite (SiC) used in sample preparation.

Observations and analyses on sample A were done at the SPECTRUM Central Analytical facility of the University of Johannesburg (UJ). Back-scattered electron (BSE) imaging and Energy Dispersive Spectrometry (EDS) analyses on sample A were carried out using a Tescan Vega3 scanning electron microscope (SEM) equipped with an Oxford Instruments XMax 50 mm^2 102 EDX detector. Some areas with high abundances of Ni-, P- and Fe-, S- rich compounds were additionally X-ray mapped. The conditions for mapping were 20 kV accelerating voltage, between 14 and 15 mm working distance and a 20nA beam current. For SEM work, no carbon coating was necessary as the material proved to be sufficiently electrically conductive; this allowed qualitative mapping of carbon. In quantitative EDS analyses and semiquantitative mapping a standardless procedure in the manufacturer-provided software was used, based on a database of peakshapes. Electron microprobe wavelength dispersive (WDS) analyses of Ni-, P- and Fe-, S- rich compounds in the sample were carried out using a CAMECA SX100 electron microprobe. Analytical conditions were 20 kV accelerating voltage, 20nA beam current, counting times of 50 s for each element, and spot sizes of 5–10 μm. These analyses used the following calibration materials: gallium phosphide for P, metallic nickel for Ni, and pyrite for Fe and S. For microprobe studies the sample was coated with carbon in vacuum.

In Potsdam BSE and EDS studies (including element mapping and quantitative analyses) were carried out on sample B, using a Zeiss Gemini Ultra Plus scanning electron microscope equipped with a Thermo Fischer Ultra Dry model 2252C-IUES-SN energy dispersive analyzer. Acceleration Voltage was 20 kV, current 200nA (field emission) and working distances between 11.9 and 15 mm. For quantitative EDS analyses a 5 μm spot size was used. Sample B was coated with a thin layer of gold prior to SEM-EDS analyses, which used a standardless procedure as at UJ.

Particle Induced X-ray Emission (PIXE) analyses on sample B were performed using the nuclear microprobe at the Materials Research Department of iThemba LABS, Somerset West, South Africa. This makes use of a 6 MV single-ended Van de Graaff accelerator. A proton beam of 3.0 MeV energy, ~200 pA current and 5 × 5 μm^2 spot size was scanned over selected areas of samples with up to 12 8 × 128 pixels. Spectra were recorded with a Si(Li) detector (30 mm^2 active area, working distance 24 mm) at a take-off angle of 135° with a 125 μm thick Be absorber. The normalisation of results was done using the integrated beam charge collected from the insulated specimen holder. Specific details are given in Andreoli et al. (2015).

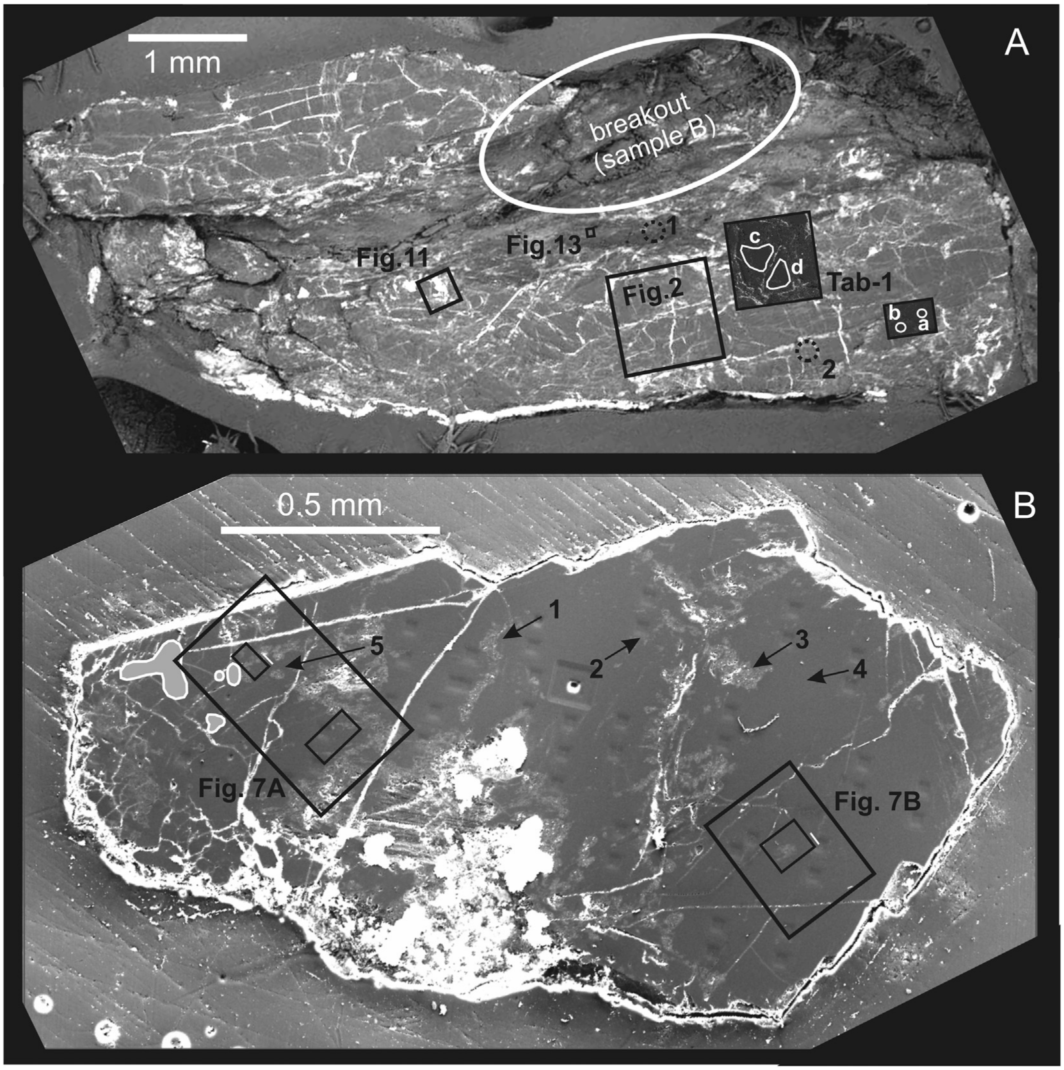

Fig. 1. backscattered electron (BSE) images of the two polished sections studied. **A**: sample A; **B**: sample B. Note the fractures that pervade the sample, highlighted by greater BSE-brightness indicating dominance of elements heavier than carbon (Si, Al, Ca). Marked in A: outlines of Figs. 2, 11 and 13; circles 1 and 2 (stippled outline) are localities of Raman spectra for graphite and SiC, respectively. White-outlined shapes a-d in darker rectangles marked "Tab 1" are localities of analyses in Table 1, on a new surface after repolishing, about 100 μm below main surface. In B, very bright areas are depressions in surface and cracks where gold coating from an earlier experiment remains. Patches of Matrix-2 in Matrix-1 are clearly visible. Outlines of Fig. 7 A and B are shown. Arrows 2 and 3 give locations of close-up BSE images and EDS element maps (Figs. 3 and 4), 1–5 give those additionally referred to in Tables 1 and 2. Light grey areas outlined in white at left side of figure show locations of PIXE analyses of Andreoli et al. (2015), which were carried out prior to the repolishing of sample B. These yielded highly anomalous data including up to 4‰ Ir and up to 0.6‰ Os, without any distinct phases being visible in BSE.

Raman spectroscopy on both samples was carried out in the Assore Raman laboratory at UJ's Geology Department, using a WITec Alpha 300R confocal Raman microscope with a frequency-doubled continuous Nd-YAG laser (532 nm) operated at between 0.5 and 1 mW for carbonaceous matrix and graphite analysis, and up to 45 mW for silicon carbide detection. Raman spectra were collected using a spectrometer with a spectral range 100–4400 cm^{-1}, with grating types of 600 g/mm for 100–1100 cm^{-1} and 1800 g/mm for the 100–3600 cm^{-1} spectral range. Nikon objectives at 20× and 50× magnifications were used. A Si-standard (1 1 1) plate was used for beam centering and Raman spectra calibrations. For analysis of the carbon spectra, the G band was fitted with a Breit-Wigner-Fano profile, and the D-band with a Lorentzian profile (Ferrari and Robertson, 2000).

3. RESULTS

3.1. Petrographic overview: a fractured carbonaceous body

Overview images of samples A and B are shown in Fig. 1. The material is crosscut by numerous fractures in random directions, spaced about 100 μm or more apart. In the BSE image these are bright due to a dominance of elements heavier than C. The fractures appear to have been originally open and in EDS maps (Fig. 2) they can be clearly distinguished from the carbon-rich matrix (and its inclusions) by the matter filling them, which has high contents of oxygen and (generally) silica, aluminium, occasionally calcium, and a low carbon content. Using XRD, clay minerals, chlorite, calcite and goethite could be identified (Kramers et al., 2013) and these minerals qualitatively fit the chemistry observed in the fractures by EDS. The infill of the fractures is clearly secondary in nature, and appears unrelated to, and in stark chemical disequilibrium with, the carbonaceous main mass of the stone. BSE and EDS maps do not show diffuse alteration zones emanating from the fractures, so that unaffected areas ranging from 50 to 200 μm in size are common. Thus secondary alteration in the Hypatia stone differs markedly from the pervasive processes seen in carbonaceous chondrites, wherein carbonaceous matter is progressively destroyed, although the newly formed minerals (clays, carbonates and Fe-oxi-hydroxides) are not dissimilar (Bland et al., 2006). The content of fractures in Hypatia is currently the subject of a separate study. The present work focuses on features of the matrix areas unaffected by fractures. BSE and EDS imaging has revealed matrix heterogeneity as well as various non-carbonaceous mineral phases in these areas. These, as discussed below, are considered primary components of the stone, and we can conclude that they are not due to alteration processes.

3.2. Two types of carbonaceous matrix

In Fig. 2, showing a localised, well-polished surface of sample A, two varieties of matrix material can be easily discerned on the basis of differing BSE brightness. One type, making up most of the volume, is uniformly BSE-‘dark’ with only very few, isolated, BSE-‘bright’ inclusions; below, this matrix type is referred to as Matrix-1. The other type shows greater BSE- ‘brightness’, and appears mottled on the μm-scale. This appearance is partly due to resolvable

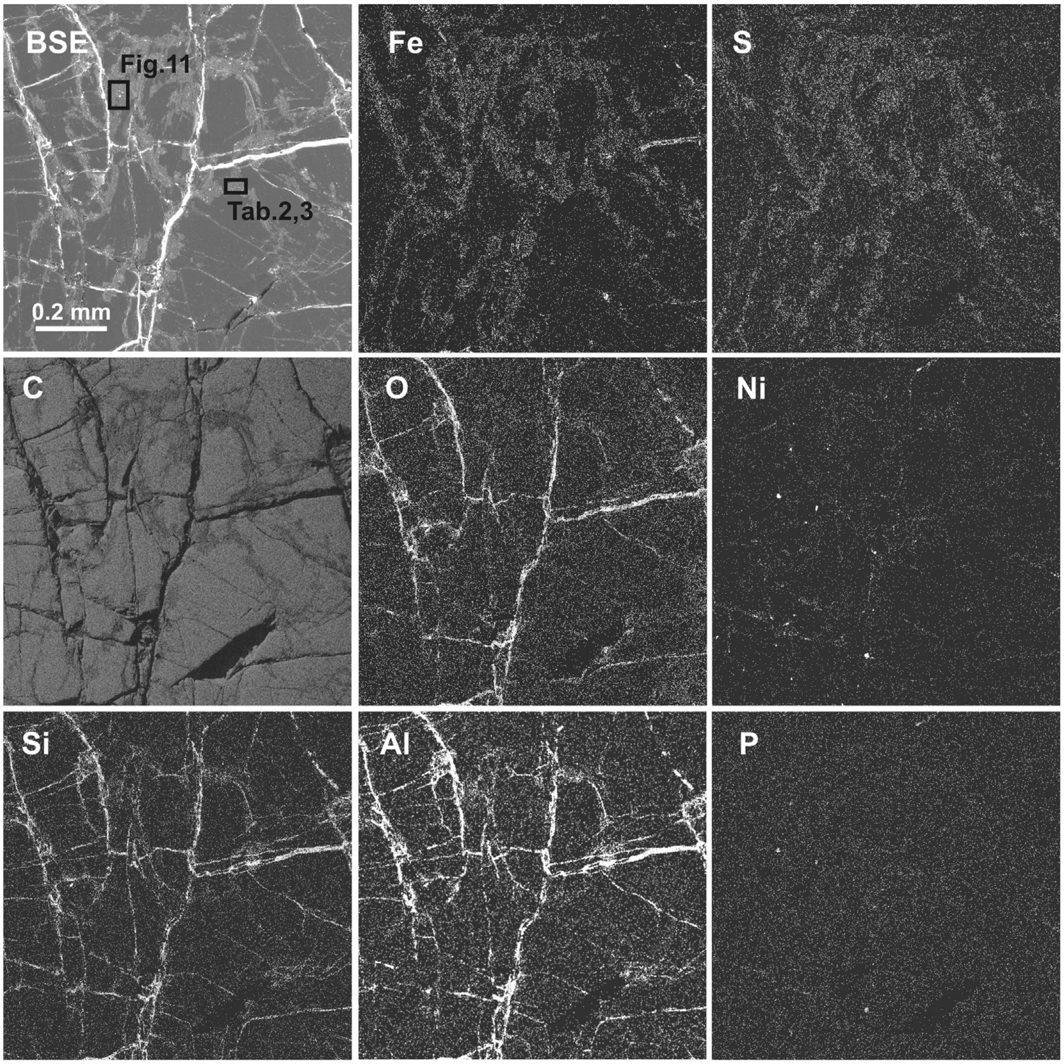

Fig. 2. BSE and selected semiquantitative EDS element maps of the region indicated on Fig. 1A. High O, Si, and Al reveal secondary phases in cracks, where C is low. Away from cracks, note the general coincidence of elevated Fe with S. Localities of Fig. 11 and analyses in Tables 2 and 3 are marked.

BSE-bright inclusions at this scale. Such inclusions are clearly visible in higher resolution images (Figs. 3 and 4) showing small BSE-brighter patches of sample B (Fig. 1B). However, the matrix in which these inclusions are embedded also has enhanced BSE- brightness relative to Matrix-1. We are unable to say if this elevated brightness is due to even smaller inclusions, that cannot be resolved using available SEM technology. This BSE-brighter matrix material with abundant inclusions is referred to below as Matrix-2. The two matrix types occur irregularly intermingled (Figs. 2–4), with Matrix-1 being dominant overall, and Matrix-2 occurring as irregular patches and streaks that typically range in width from <5 μm to ∼50 μm. No transitional matrix types were seen, and the boundaries between the two types are well defined (Figs. 2–4), in some cases marked by a 1–2 μm wide band of enhanced

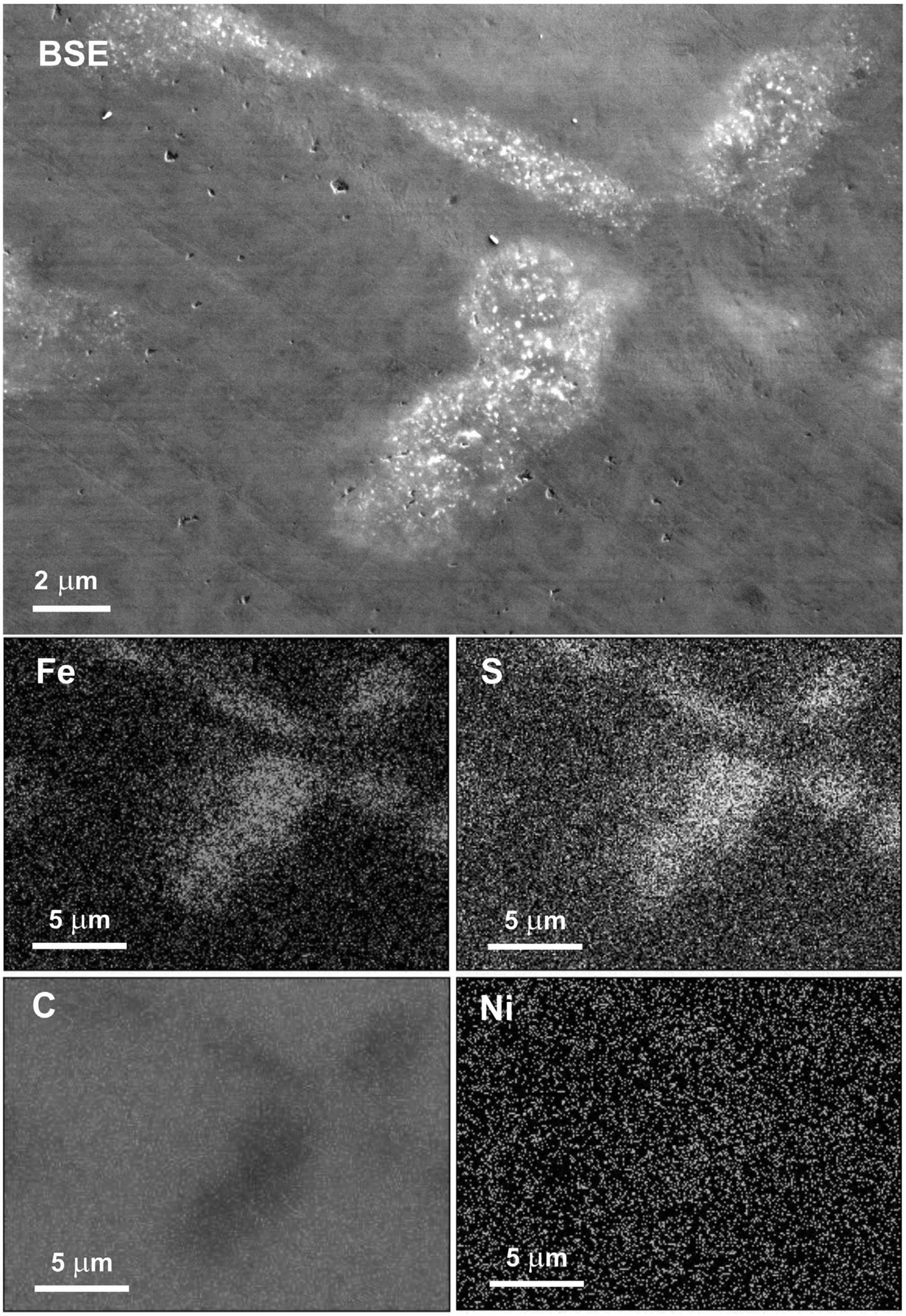

Fig. 3. BSE- and non-quantitative EDS maps of locality 2 (arrow) in Fig. 1B. View of a patch enriched in Fe and S, discrete grains visible in the BSE image but not resolved in the EDS images.

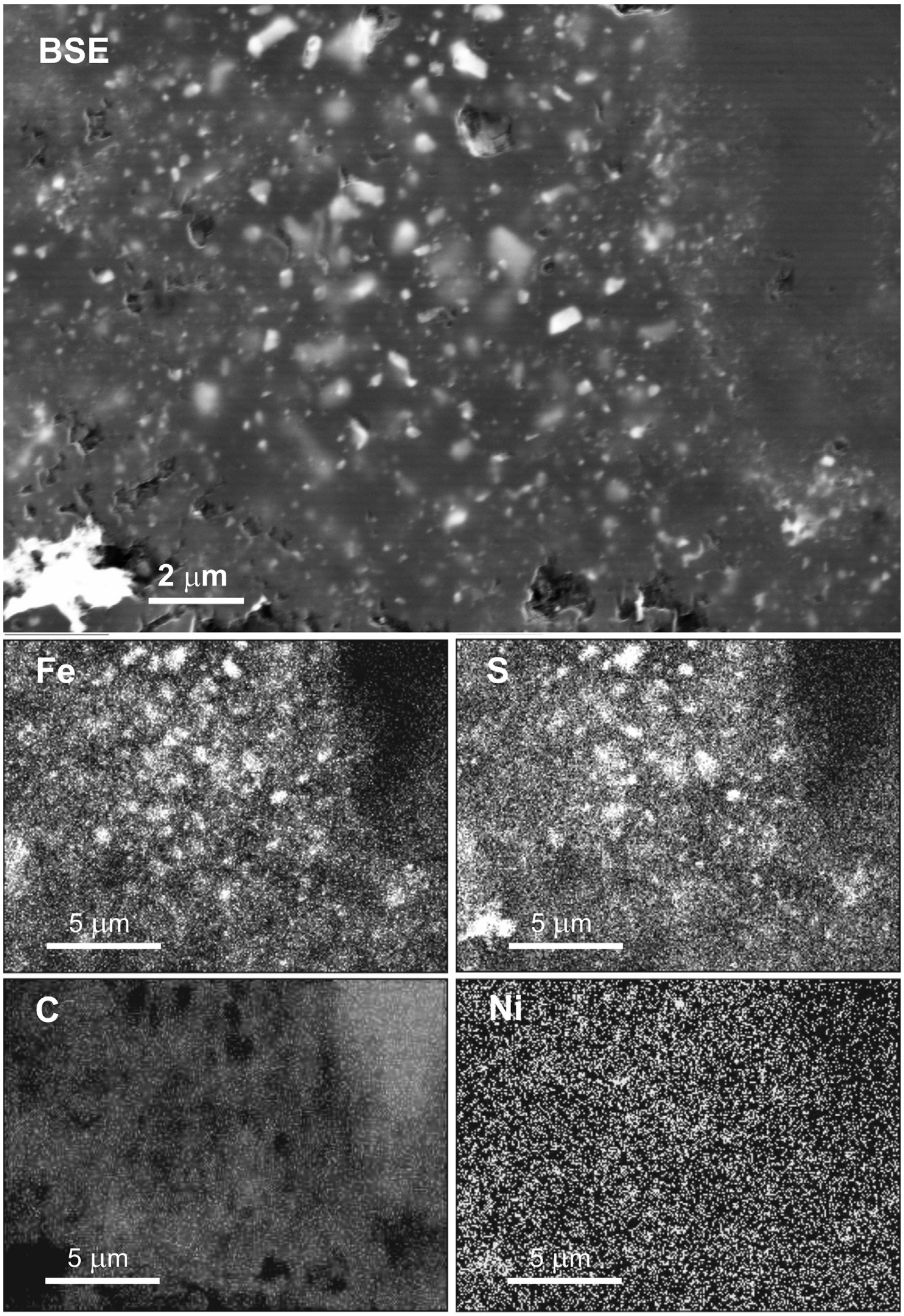

Fig. 4. BSE- and non-quantitative EDS maps of locality 3 (arrow) in Fig. 1B. BSE-bright grains are seen to consist of Fe and S, mostly without apparent enrichment in Ni.

BSE-brightness. While no alteration zone is seen to emanate from fractures, it appears that some of the larger fractures follow zones of Matrix-2 (Fig. 2). This suggests a mechanical difference, with Matrix-2 being the more brittle of the two types.

Table 1 reports four PIXE analyses in circular spots a, b and regions c, d in the darker rectangles marked ‘Tab-1′ in Fig. 1A, which lie outside Matrix-2 clouds and away from fractures. In the 50 μm spots a and b all elements except Fe, S and Ni are below detection limits (O, N and C cannot be analysed by PIXE). The larger regions c and d, with mostly lower detection limits, show higher concentrations than a and b (but nevertheless still trace levels) for most elements analysed. Furthermore, in region 4 of Sample B (Fig. 1B) which is also remote from visible Matrix-2, five out of six spot analyses carried out by SEM EDS detected

Table 1
PIXE analyses of Matrix-1 areas a-d in dark rectangles marked 'Tab 1' on Fig. 1A.

	a & b Detect. Lim.	Area a ppm ± 2SE	Area b ppm ± 2SE	c & d Detect. Lim.	Area c ppm ± 2SE	Area d ppm ± 2SE
Al	120			192	584 ± 139	596 ± 105
Si	140	<280.	<238.	37	543 ± 162	600 ± 65
P	10			17	<33.	<37.
S	39	102 ± 22	<78.	11	203 ± 11	231 ± 10
Cl	41	<59.	<53.	7	<14.	17 ± 4
K	16	<34.	<30.	4	<8.	<10.
Ca	13	<27.	32 ± 6	3.2	64 ± 8	62 ± 2
Ti	9	<19.	<16.	2.2	<4.	13 ± 2
V	1			1.8	<4.	<4.
Cr	5	<12.	<10.	1.5	6 ± 1	<3.6
Mn	5	<11.	<9.	1.4	<2.9	<3.4
Fe	5	160 ± 9	102 ± 10	1.3	721 ± 22	873 ± 16
Ni	6	17 ± 9	<11.	1.5	63 ± 2	67 ± 3
Cu	9	<20.	<18.	1.7	8.9 ± 1	5 ± 1
Zn	14	<32.	<23.	1.8	<3.7	<3.7

Note: Five SEM-EDS analyses (Potsdam) in locality 4 of sample B (arrowed in Fig. 1B) detected only C. One detected in addition 490 ppm Fe (O not analysed).

no elements except C, while one showed about 490 µg/g Fe. A comparison of these data with those from Matrix-2 (Table 2), as discussed below, reveals a large chemical difference between the two matrix types that correlates well with grey scale patterns seen on BSE images.

3.3. Iron sulphide phase and Fe, S in Matrix-2

Semiquantitative element mapping by EDS shows that the BSE-brighter Matrix-2 streaks and patches correspond to elevated Fe and S content (Figs. 2–4; Table 2). The carbon content must be correspondingly lower, although the weaker C signal in Matrix-2 compared to Matrix-1 may at least in part result from greater absorbance of the soft X-rays from C due to the higher concentration of heavier elements (Henke, 1964; Henke and Tester, 1975). Oxygen concentrations appear to be quite similar in both matrix types (Fig. 2). Some small discrete grains of high BSE-brightness, coinciding with high Ni and P abundances, are discussed further below.

Fig. 3 (arrowed locality 2 in Fig. 1B) shows a small Matrix-2 cloud with BSE-bright grains that reach sizes up to 0.5 µm in the interior of the cloud, while its edge only shows grains smaller than 0.1 µm. Fig. 4 (locality 3 in Fig. 1B) shows a Matrix-2 area with grains up to 1 µm, which are resolved by EDS mapping as consisting of Fe and S, with no noticeable enrichment of Ni in the grains. These appear to have a crystalline shape although no symmetry group could be determined.

The results of WDS electron microprobe analyses (sample A, UJ) and quantitative high spatial resolution EDS analyses (sample B, Helmholtz Zentrum Potsdam) are listed in Table 2. Spot sizes between 5 and 10 µm in the Matrix-2 patches contain between 1 and 8 wt.% of Fe, Ni, P and S combined, thus implying >90 wt.% of (oxygen-bearing) carbonaceous matter. The atomic (Fe + Ni)/S ratios obtained in the WDS analyses at UJ and the EDS analyses at Potsdam define the same range, mostly between 1.3 and 2.0, with a few outliers up to 6.15. The overall average is 1 .51 ± 0.24 (1SD). Atomic Ni/Fe ratios in the WDS analyses on sample A range from 0.08 to 0.41, whereby the higher values obtained are associated with high P/S ratios and thus most likely reflect small Ni, P rich grains in the analysed spots (see below). The Potsdam EDS analyses of regions in sample B containing the Fe sulphide phase (localities 1, 3 and 5 in Fig. 1B), where no Ni, P rich grains were observed, produced Ni/Fe ratios ranging from 0.03 to 0.14. The average value of all analyses is 0.086 ± 0.061 (1SD).

Clearly these spot- and region analyses can include Fe, Ni and S in the carbonaceous matter as well as the Fe-sulphide inclusions. Since the mineral pyrrhotite cannot have atomic (Fe + Ni)/S ratios higher than unity (the ratio for troilite), and there is no known sulphide phase with $Fe \gg Ni$ and $(Fe + Ni)/S > 1$, we conclude that the Fe-sulphide phase is most likely pyrrhotite with a composition close to troilite, and suspect that the excess Fe and Ni (and possibly some S) indeed reside in the carbonaceous matrix. Plots of S and Ni vs. Fe content (Fig. 5) show good collinearity for both element pairs at low concentrations, while at higher concentrations there are deviations that appear to indicate Fe excess, S deficiency in some points, and marked Ni excess in two EMPA points (discussed below). Broadly, however, the S/Fe and Ni/Fe ratios found remain constant over a large range of Fe content (ranging from 0.5 to 7 wt.% Fe).

Interestingly, the average (Fe + Ni)/S and Fe/Ni ratios of Matrix-2 are close to the values of both CI chondrites and the Sun. On the other hand, the estimated Fe/C atomic ratio for Matrix-2 (obtained using the assumption that the carbonaceous matrix contains 5% oxygen and other elements apart from those analysed) is lower than the solar and CI values by one and two orders of magnitude, respectively (Table 2; Palme and Jones, 2003).

Table 2
Analytical data on Matrix-2 with (Fe, Ni) sulphide phase: EMP and SEM-EDS data.

						Atomic ratios			
	Point #	P	S	Fe	Ni	(Fe + Ni)/S ± 1 SE	Ni/Fe ± 1 SE	P/S ± 1 SE	Fe/C**
Sample A, see Fig. 2 (UJ-EMPA, WDS, wt%)									
(Detection limit)		(0.012)	(0.012)	(0.018)	(0.02)				
	6	0.06	1.63	3.52	0.65	1.50 ± 0.04	0.176 ± 0.010	0.039 ± 0.007	0.008
	7	0.03	2.35	4.69	0.56	1.32 ± 0.03	0.114 ± 0.008	0.014 ± 0.005	0.011
	11	0.12	1.36	3.2	1.37	1.96 ± 0.06	0.407 ± 0.014	0.094 ± 0.008	0.008
	20	0.02	2.04	4.49	0.41	1.42 ± 0.04	0.087 ± 0.009	0.010 ± 0.005	0.011
Sample B, locality 1 of Fig. 1B (Helmholtz, EDS, wt%)									
(Detection limit)			(0.05)	(0.04)	(0.03)				
	H-2-1		0.39	1.09	0.1	1.80 ± 0.12	0.087 ± 0.006		0.003
	H-2-2		0.27	0.67	0.06	1.59 ± 0.10	0.085 ± 0.006		0.002
	H-2-3		0.86	2.96	0.26	2.21 ± 0.14	0.084 ± 0.003		0.007
	H-2-4		0.35	0.92	0.08	1.69 ± 0.11	0.083 ± 0.008		0.002
Sample B, locality 3 of Fig. 1B (Helmholtz, EDS, wt%)									
	H-5-1		2.68	7.17	0.51	1.69 ± 0.11	0.068 ± 0.006		0.018
	H-5-2		2.58	6.06	0.27	1.45 ± 0.09	0.042 ± 0.006		0.015
	H-5-3		2.91	6.91	0.22	1.45 ± 0.09	0.030 ± 0.005		0.017
	H-5-4		2.18	4.32	0.15	1.21 ± 0.08	0.033 ± 0.009		0.010
	H-5-5		1.93	4.06	0.17	1.30 ± 0.08	0.040 ± 0.009		0.010
	H-5-6		1.37	4.86	0.47	2.29 ± 0.15	0.092 ± 0.008		0.012
	H-5-10		0.37	0.75	0.08	1.32 ± 0.10	0.101 ± 0.051		0.002
	H-5-11		0.48	1.08	0.08	1.43 ± 0.10	0.070 ± 0.035		0.002
	H-5-12		0.61	1.34	0.11	1.40 ± 0.10	0.078 ± 0.028		0.003
	H-5-13		0.56	1.28	0.08	1.43 ± 0.10	0.059 ± 0.030		0.003
	H-6-1		0.74	1.69	0.13	1.45 ± 0.10	0.073 ± 0.023		0.004
	H-6-2		0.59	1.27	0.13	1.40 ± 0.10	0.097 ± 0.030		0.003
	H-6-3		0.62	1.47	0.15	1.54 ± 0.10	0.097 ± 0.026		0.003
	H-6-4		0.73	1.68	0.16	1.49 ± 0.10	0.091 ± 0.023		0.004
	H-6-5		0.72	1.75	0.16	1.56 ± 0.10	0.087 ± 0.022		0.004
	H-6-6		0.7	1.59	0.13	1.45 ± 0.10	0.078 ± 0.024		0.004
	H-6-7		0.67	1.55	0.1	1.45 ± 0.10	0.061 ± 0.024		0.004
	H-6-8		*0.72*	*6.55*	*0.97*	*6.15 ± 0.39*	*0.141 ± 0.006*		*0.016*
	H-6-9		*1.29*	*5.61*	*0.74*	*2.90 ± 0.18*	*0.126 ± 0.007*		*0.014*
	H-6-10		1.13	2.19	0.12	1.21 ± 0.08	0.052 ± 0.017		0.005
	H-6-11		0.63	1.37	0.11	1.39 ± 0.10	0.076 ± 0.028		0.003
	H-6-12		1.31	3.29	0.21	1.58 ± 0.10	0.061 ± 0.012		0.008

(*continued on next page*)

Table 2 (*continued*)

Point #	P	S	Fe	Ni	Atomic ratios (Fe + Ni)/S ± 1 SE	Ni/Fe ± 1 SE	P/S ± 1 SE	Fe/C[**]
Sample B, locality 5 of Fig. 1B (Helmholtz, EDS, weight%)								
H-8-1		1.53	3.47	0.18	1.41 ± 0.09	0.049 ± 0.011		0.008
H-8-2		1.7	4.31	0.22	1.57 ± 0.10	0.049 ± 0.009		0.010
H-8-3		0.59	1.3	0.11	1.41 ± 0.10	0.081 ± 0.029		0.003
H-8-4		0.54	1.13	0.1	1.34 ± 0.10	0.084 ± 0.034		0.003
H-8-5		0.49	1.03	0.07	1.33 ± 0.10	0.065 ± 0.037		0.002
H-8-6		0.43	0.93	0.07	1.37 ± 0.10	0.072 ± 0.041		0.002
H-8-7		0.35	0.7	0.08	1.31 ± 0.11	0.109 ± 0.055		0.002
H-8-8		0.66	1.65	0.14	1.60 ± 0.11	0.081 ± 0.023		0.004
Average of ratios ± 1 SD[*]					1.51 ± 0.24	0.086 ± 0.061	0.039 ± 0.039	0.006
Ratio CI (Palme and Jones, 2003)					2.06	0.055	0.018	1.23
Ratio sun (Palme and Jones, 2003)					1.40	0.063	0.013	0.115

Detection limits in brackets.

Uncertainties (1 SE): EMPA, P: 0.01 (abs), Ni: 0.015 (abs.), S: 2.5%, Fe: 0.9%, SEM-EDS, Ni: 0.04 (abs) S: 6%, Fe: 2%.

[*] Excluding outliers shown in italics, probably affected by Ni-phosphide grains.

[**] C abundance derived by assuming that the carbonaceous matrix contains 5% oxygen and other elements apart from those analysed.

3.4. Raman spectroscopy of the carbonaceous matrix types

Sample B provided sufficiently large flat areas for micro-Raman spectroscopy, including mapping. Raman bands are weakly developed and superimposed on a fluorescence background that shows a broad maximum between wavenumbers (wn) 2500 and 3000 cm^{-1} corresponding to wavelengths between 614 and 633 nm for an excitation wavelength of 532 nm. This fluorescence maximum is in the range of that found for CI and CM chondritic insoluble organic matter (IOM; Bonal et al., 2005). Typical examples of our Raman spectra are shown in Fig. 6. Matrix-1 is characterised by the D and G bands typical of sp^2 bonds in disordered carbon (Ferrari and Robertson, 2000), with G bands somewhat higher than D bands. The D-G band spectra and fluorescence superficially resemble those obtained from dust particles retrieved by the 'Stardust' mission to Comet 81P/Wild. (Fig. 6; Sandford et al., 2006; Rotundi et al., 2008) and interplanetary dust particles (Allamandola et al., 1987; Quirico et al., 2005), although the D-bands appear narrower than in these published spectra and have a curious sharp edge on their low-wavenumber side. In the Matrix-2 spectra, a discrete narrow band of variable intensity appears superimposed on the D band at 1340 cm^{-1}. As this becomes more prominent, normal D and G bands weaken and appear broader; in some cases they disappear completely. This narrow band is consistent with the sp^3 bonds of diamond, although it is displaced to somewhat higher wn from the typical value of 1332 cm^{-1} (RRUFF database, Lafuente et al., 2015). Typically, the fluorescence background for Matrix-2 is also different, showing higher intensity at low wavenumbers and a high, narrower peak at wn between 3100 and 3500 (637 and 654 nm for excitation at 532 nm). Minor peaks occasionally detected between wn 200 and 1200 are not reproduced between spectra, and cannot be connected to minerals. Specifically, no sulphide phases could be identified in our Raman spectra (RRUFF database, Lafuente et al., 2015).

Attempts at fitting the G-Band with a Breit–Wigner-Fano profile, and the D-band with a Lorentzian profile (Ferrari and Robertson, 2000), revealed that none of the carbon spectra from Matrix-1 could be modelled with the sp^2 D and G bands alone, due to the sharp edge on the D band. Adding a third band with wavenumber and width similar to those of the prominent diamond bands in Matrix-2 spectra (also with a Lorentzian profile) allowed satisfactory fits (Fig. 6, top), indicating that the apparent D band in Matrix-1 is a composite and a phase with sp^3 carbon (diamond or diamond-like carbon) is also present in Matrix-1.

The results of semiquantitative mapping of Raman G and "composite" or combined D + sp^3 intensities band intensities in three areas of sample B are shown in Fig. 7. The areas were selected on the basis of good polish, strong contrasts in BSE-brightness and the absence of fractures. Our Raman mapping yields two important observations, which apply to all three areas. First, the intensities of the "composite D" and G bands are anticorrelated. Second, regions of high "composite D" band intensity coincide with BSE-bright zones, i.e. Matrix-2.

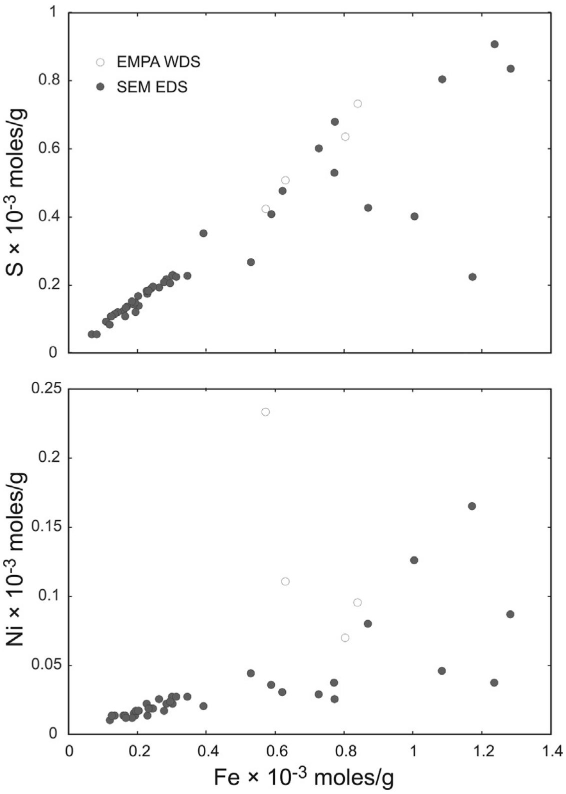

Fig. 5. plots of S and Ni vs. Fe in millimoles/g for all EMPA and SEM-EDS analyses of areas relatively enriched in Fe, S and Ni. Note generally good correlations for low concentration points and regions. Deviations at higher concentrations, occurring in either plot but not in both, therefore indicate excess or deficiency in Ni or S.

Our reflected light images show that the variations in chemistry revealed by the BSE images do not cause contrasts in reflectivity or apparent quality of the polish, which indicates homogeneous hardness. Since the three-band fitting of Matrix-1 spectra has shown that diamond is ubiquitous in both types of matrix, this is not surprising. Moreover, in Raman spectroscopy using visible light excitation, the detection cross section of sp^2 bonds is at least 50 times greater than that of sp^3 bonds (Ferrari and Robertson, 2000). This means that diamond is most likely an important or even dominant phase in Matrix-1 as well, suggesting that diamond is responsible for the hardness of both matrix types. Meanwhile the observed electrical conductivity of both matrix types indicates that a connected network of non-diamond carbon is present throughout (see supplementary information to Avice et al., 2015; Fig. 2D of Kramers et al., 2013).

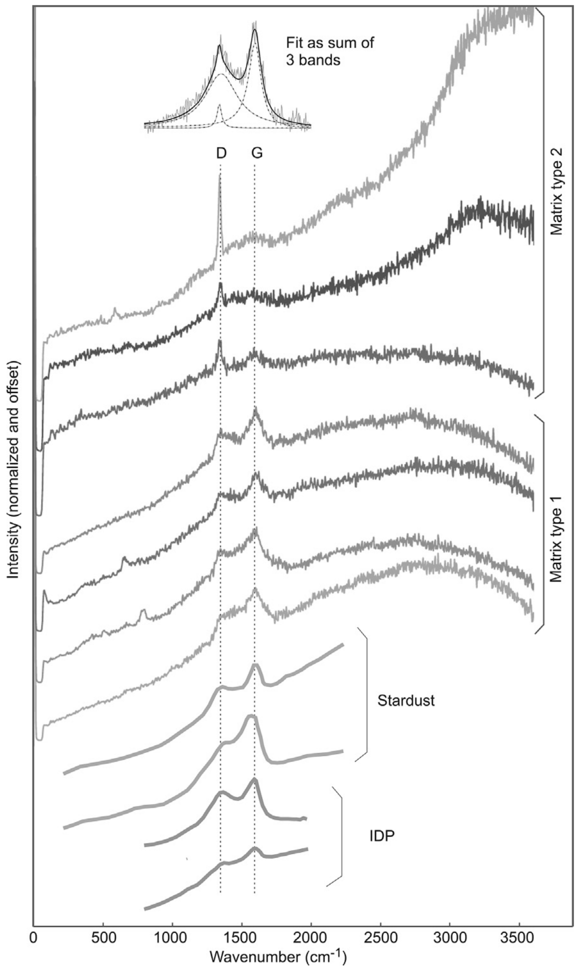

Fig. 6. Examples of Raman spectra for Hypatia matrix types 1 and 2 over wavenumbers (wn) of 0 to 3600 cm^{-1} showing G and D bands superimposed on fluorescence background. Spectra from Comet Wild2 stardust (Sandford et al., 2006) and interplanetary dust particles (Rotundi et al., 2008) shown for comparison, also without background subtraction. Hypatia spectra are shown normalised to (intensity at 1600 cm^{-1}) = 100 units and offset from each other by 35 units. Other spectra are scaled to enable comparison. Relative intensity of background at low wavenumbers is shown by subvertical lines at wn = 60. Stippled reference lines "D" and "G" are at wn of 1350 and 1600 cm^{-1} respectively. Note emergence of the narrow diamond sp^3 band in Matrix-2 as the G band is weakening and becoming broader. Fluorescence in Matrix-1 peaks at 614–633 nm; background in Matrix-2 is higher at low wavenumbers and the strong fluorescence peaking at c. 637–654 nm seen in two spectra is typical. WITec Alpha 300R Raman microscope, laser wavelength 532 nm; laser power 0.6 mW. Image at top shows curve fitting with three bands after baseline subtraction.

Plots of $FWHM_D$ vs. I_D/I_G values and $FWHM_G$ vs. wn_G values obtained from Matrix-1 spots in the Raman-mapped areas of Sample B by our three-band analysis are shown in Fig. 8A and B, respectively (orange dots). For Matrix-2, no reliable D-G or G parameters could be obtained due to the weakness of the bands and the prominent diamond sp^3 signal. Noting that, in the case of graphite, polishing may enhance the intensity of the D band relative to the G band (Beyssac et al., 2003), we have also obtained spectra from untreated fracture surfaces of grains of Hypatia for comparison. The signals from D and G bands are much weaker than on the polished surface and in many cases not significantly above noise level. An sp^3 band of varying intensity is seen in all cases. Data obtained from 6 spectra with low sp^3 band intensities (thus probably

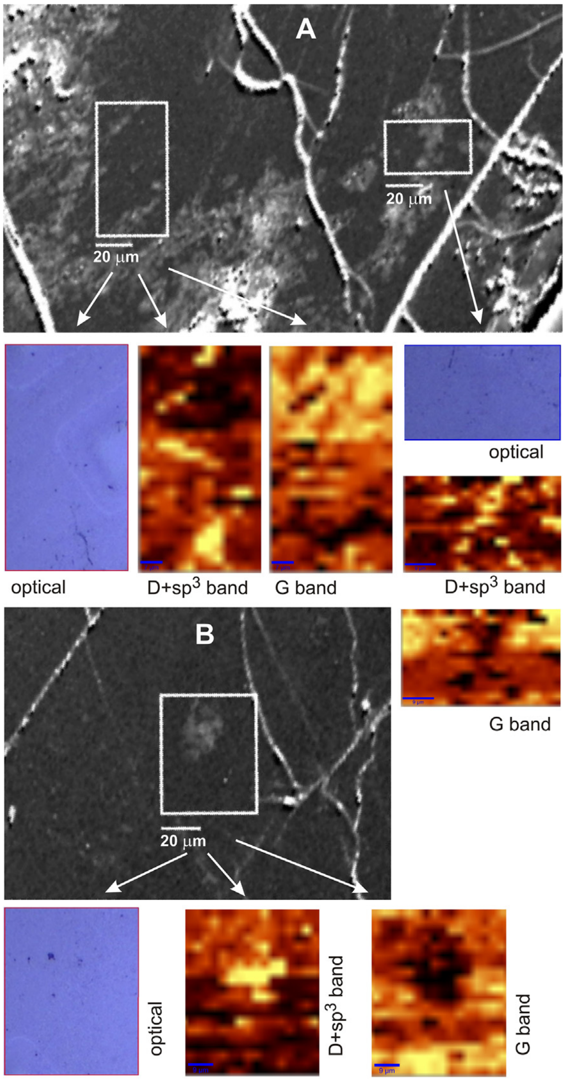

Fig. 7. BSE images of rectangular regions shown in Fig. 1B with optical images and semiquantitative "composite" ($D + sp^3$) band and G band maps of areas indicated within them. Combined ($D + sp^3$) band values for mapping were obtained by integrating signal intensities in the wn range 1322–1363 cm^{-1} relative to the background at these limits, and G-band values analogous over 1573–1620 cm^{-1}. High ($D + sp^3$) band and low G band intensities are seen to be associated with BSE-bright regions (Matrix-2). Optical images do not show any difference between matrix types 1 and 2 on the polished surface. Spectra for mapping taken 2 µm apart in both X and Y directions. WITec Alpha 300R Raman microscope, laser wavelength 532 nm; laser power 0.6 mW.

from Matrix-1) are also shown in Fig. 8A and B (brown dots with error bars). For these fracture surfaces, the FWHM values for both D and G bands are at the upper limit of the range for the more precise data from the polished surface, and the wn_G range extends to somewhat lower values. However, the data from fracture surfaces do not fundamentally differ from those obtained on polished surfaces.

Fig. 8A and B further show a comparison with the carbonaceous matter of various types of solar nebula objects. As the values for the measured parameters vary significantly with the excitation wavelength (Starkey et al., 2013), the comparison is limited to data obtained with green light (532 and 514.5 nm); further, the energy in all cases was 1 mW or less, similar to our analyses. For Hypatia's Matrix-1, both I_D/I_G and $FWHM_D$ values (Fig. 8A) are close to those of primitive CI, CM and CR chondrites, IDP's (Quirico et al., 2005, 2014; Dobrică et al., 2011; Starkey et al., 2013), ultracarbonaceous Antarctic micrometeorites (UCAMM's, Dobrică et al., 2011) and Stardust material (Sandford et al., 2006; Rotundi et al., 2008). In the plot of $FWHM_G$ vs. wn_G (Fig. 8B) the Matrix-1 data overlap the fields defined by these same types of least-processed solar system material (Quirico et al., 2005; Busemann et al., 2007; Dobrică et al., 2011; Starkey et al., 2013) although the very low values of wn_G found for some extremely primitive IDP's (Busemann et al., 2009) and Stardust are not reached. In both plots there is a clear separation from the fields defined by ordinary chondrites (Quirico et al., 2003; Busemann et al., 2007; Starkey et al., 2013; Bonal et al., 2016), CV chondrites (Bonal et al., 2006, 2016; Busemann et al., 2007) and CO chondrites (Bonal et al., 2007, 2016; Busemann et al., 2007).

The I_D/I_G intensity ratios smaller than unity in Matrix-1 suggest the prevalence of complex disordered carbon consisting of large aromatic skeletons with other functional groups, as found in IDP's, carbonaceous chondrites and also terrestrial coals (e.g. Quirico et al., 2003, 2005, 2009; Kouketsu et al., 2014). Polyaromatic hydrocarbons (PAH's), which might exist in the disordered carbon, are an important component of interstellar carbonaceous matter (Allamandola et al., 1987; Quirico et al., 2005). The apparent coexistence of similar matter with probably shock-induced diamond (Kramers et al., 2013; Avice et al., 2015) is remarkable.

3.5. Graphite

Graphite has previously been reported in Hypatia by Barakat (2012) from XRD data, and by Avice et al. (2015) as <10 nm sized domains apparently coating diamond grains. In the area indicated as circle 1 (with stippled outline) in Fig. 1A, a poorly polished region of Matrix-2, a ca. 80 µm cluster of discrete grains occurs, individually up to about 8 µm in size and optically highly reflective depending on their orientation (Fig. 9A and B). The Raman spectrum is unequivocally that of graphite (Fig. 9C; Reich and Thomsen, 2004). It further differs from the matrix spectra (Fig. 6) in that there is only a weak fluorescence background. A low intensity D band in graphite is common, and results from defects. In the present case its position at 1335 cm^{-1} raises a question, as the D peak in "defective" graphite for a 532 nm excitation normally occurs at 1350 cm^{-1} or higher (Reich and Thomsen, 2004). The apparent D band in Fig. 9C is rather close to the sp^3 diamond peaks seen in the matrix spectra, and the co-occurrence of diamond with this graphite can therefore not be excluded. On the polished surface, this cluster forms a deep pit. We suspect that graphite may be easily lost in polishing, being very soft compared to the diamond-bearing matrix.

Although this cluster represents the only occurrence confirmed by Raman spectroscopy so far, graphite may therefore be more common than our data suggests.

Graphite occurs in iron meteorites, (Vdovykin, 1973; Scott and Goldstein, 2012) as well as in achondrites of the acapulcoite-lodranite group (Avice et al., 2015), in enstatite chondrites (Rubin, 1997) and in unequilibrated chondrites. In the latter it forms aggregates up to ca. 1 mm in size and with grain sizes up to ca. 50 µm (Mostefaoui et al., 2005). Presolar graphite occurs in chondrites in abundances less than 30 µg/g, as grains up to ca. 5 µm but usually much smaller. Although graphite has been observed *in situ* only once, in a CO chondrite (Haenecour et al., 2015), it has been separated and identified via its anomalous noble gas and carbon isotope ratios (Huss and Lewis, 1995; Huss et al., 2003; Croat et al., 2003).

3.6. Silicon carbide

Although clay minerals and other silicates are commonly found in the cracks within the Hypatia stone, the Si-content of the carbonaceous matrix itself is quite low (Table 1). This allows small Si-rich grains to be located using EDS element mapping. Small grains with high Si content and without oxygen were found in five locations of sample A, all of these were associated with Matrix-2, and all in regions relatively rich in Ni-phosphide grains.

In circle 2 (with stippled outline) of Fig. 1A a grouping of Si-rich, O-free grains was identified. In Fig. 10A and B, optical and BSE images are shown; two adjacent 5 µm grains along with a smaller grain (locality 1) appear to be fragments of a single broken grain. Two Raman spectra (Fig. 10C and D) acquired at localities 1 and 2 (Fig. 10A

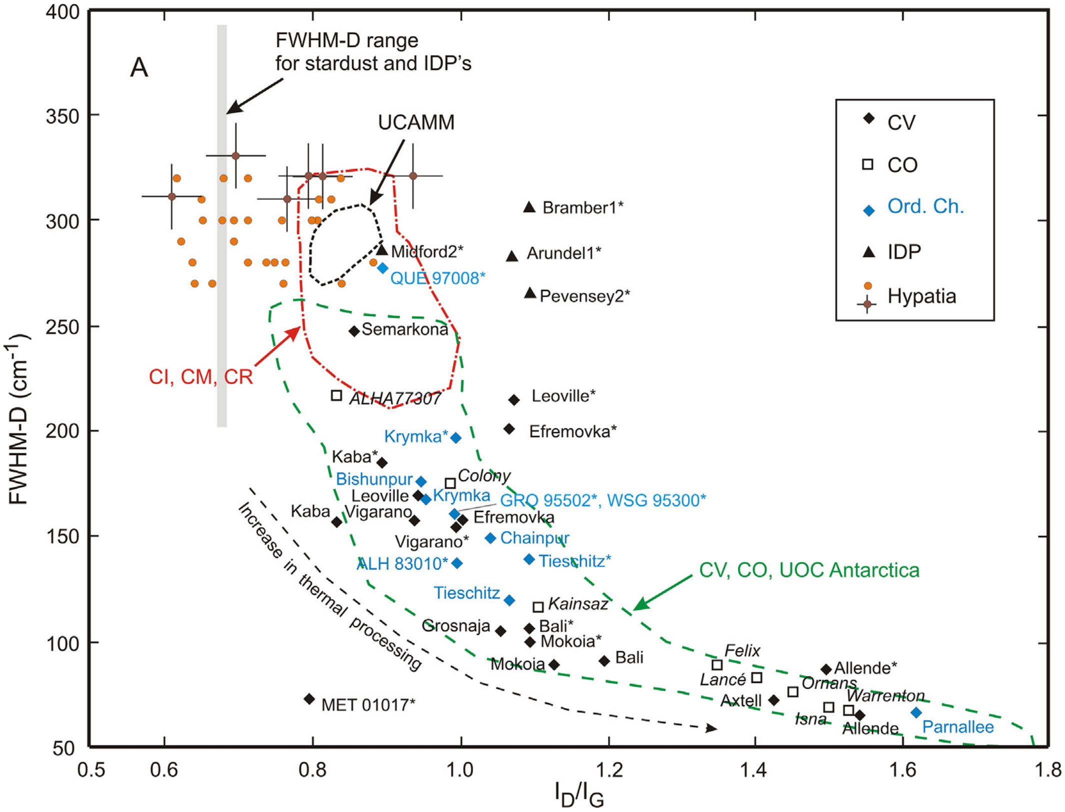

Fig. 8. D- and G band characteristics of 2 µm diameter spots on the polished surface of Hypatia carbonaceous Matrix-1 in sample B (orange dots) and fracture surfaces of grains (brown dots with 1σ error bars), compared to data from various extraterrestrial carbonaceous matter. **A:** Full Width at Half Maximum (FWHM, in cm^{-1}) of the D band vs. amplitude ratio I_D/I_G of the D and G bands. Data for individual OC's, CV's and CO's from Quirico et al., 2003; Bonal et al., 2005, 2007; Starkey et al., 2013 (asterisks). Dashed green curve "CV, CO, UOC Antarctica" outlines field defined by 100 chondrites of these types from NASA's Antarctic collection (Bonal et al., 2016). Fields for CI, CM, CR (Quirico et al., 2005, 2014; Dobrică et al., 2011; Starkey et al., 2013). chondrites and UCAMM (ultracarbonaceous Antarctic micrometeorites, Dobrică et al., 2011) indicated. The range in FWHM-D values for dust particles returned from Comet 81P/Wild2 by NASA's "Stardust" mission (Sandford et al., 2006; Rotundi et al., 2008) and IDP's (Quirico et al., 2005) is shown by a grey bar; their I_D/I_G values are not reported but are <1 from figures in the publications. Individual IDP data from Starkey et al. (2013). **B:** FWHM vs. centre wavenumber of the G band (both in cm^{-1}), compared to data from other extraterrestrial IOM. Data sources as in A; additionally for OC's, CV's and CO's, Busemann et al. (2007), Bonal et al. (2016) and for IDP's Busemann et al. (2009). Error bars are from the sources. Note that no diamond sp^3 band was present in any of the published spectral data shown. Also, most of these represent averages of 10 or more measurements, while the Hypatia points represent single measurements, which explains their relatively wide spread. However, all data were acquired with either 514.5 nm or 532 nm excitation wavelength, and spectrum fitting using Lorentzian profiles for the D band and Breit-Wigner-Fano profiles for the G band, as done in this study. Thus while fine details should be observed with caution, the broad comparisons are considered to be valid.

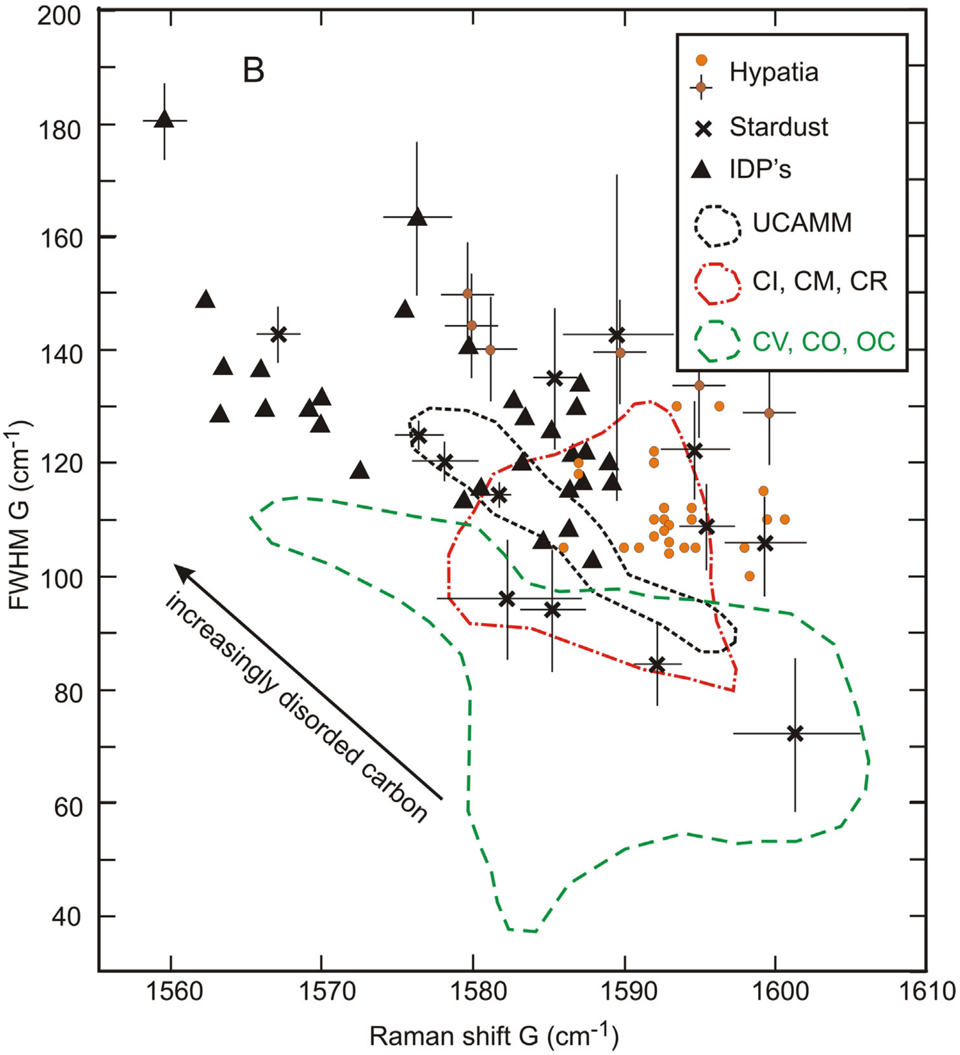

Fig 8. *(continued)*

and B) using very high laser power (45 mW), both reveal the main diagnostic peak for moissanite (SiC) at 790–799 cm^{-1}. The presence of a single main band, as observed, is characteristic of the cubic moissanite variety, βSiC (Virag et al., 1992). The hexagonal or rhombohedral polytypes (αSiC) appears to be excluded due to the absence of a resolvable band at ca. 770 cm^{-1}. The minor band at 985 cm^{-1} seen in Fig. 10C, and absent in Fig. 10D occurs in only one of the 5 spectra obtained from large βSiC grains from the Murchison meteorite by Virag et al. (1992). The high laser power caused a high fluorescence background from the carbonaceous matrix, and Fig. 10C also shows the broad D and G bands discussed above in Section 3.4. Semiquantitative EDS maps for Si, C and O are shown in Fig. 10E–G. Oxygen is related to a small fracture (Fig. 10B). Little or no X-rays from carbon were detected from within the SiC grains. We suggest this is due to strong absorption, in the mineral itself, of the soft X-rays from carbon (Henke, 1964; Henke and Tester, 1975).

Moissanite is a common trace constituent in chondritic meteorites, and is considered to be mostly of presolar origin, with an abundance estimated at 15–30 μg/g and grainsizes up to about 5 μm (Huss and Lewis, 1995; Davidson et al., 2014) although rare grains >10 μm (Virag et al., 1992) and even up to 30 μm (Zinner et al., 2011) have been studied, the latter representing a poly-grained aggregate. While moissanite has been observed *in situ* in chondritic meteorites via isotopic anomalies (Floss and Stadermann, 2009), it has commonly been recovered and identified (as is the case with insoluble organic matter, presolar graphite and diamonds) by dissolving the bulk matter using mixtures of fluoride salts and HF (Virag et al., 1992; Anders and Zinner, 1993; Lewis et al., 1994; Davidson et al., 2014).

3.7. Nickel phosphide compound

A fairly common type of inclusion in the carbonaceous matrix of Hypatia is rich in both Ni and P, with minor Fe, and poor in O. Such material is BSE-bright and mostly forms small grains (<10 μm, Figs. 2 and 11) which correlate with the Ni-rich anomalies seen in Table 2 and Fig. 5. These

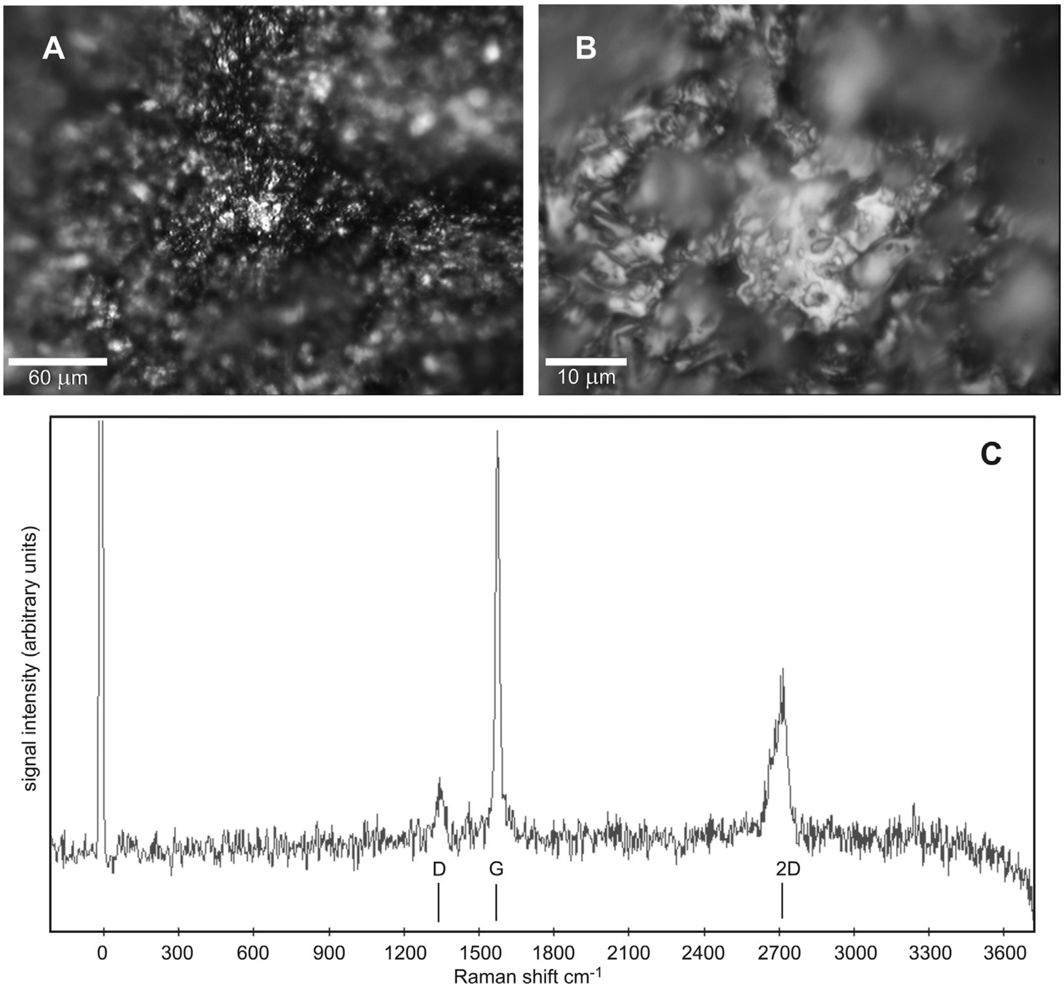

Fig. 9. Cluster of graphite grains, locality shown as circle 1 in Fig. 1A. **A** and **B**, optical images in different magnifications, showing granular texture. **C**, Raman spectrum showing pronounced G band at 1580 cm^{-1} and 2D band at 2700 cm^{-1}. The band at 1335 cm^{-1} may be a D band indicating disorder (Reich and Thomsen, 2004), or may reflect the presence of diamond. WITec Alpha 300R Raman microscope, Excitation wavelength 532 nm, power 1 mW.

inclusions are rare and isolated in Matrix-1, but quite common in Matrix-2 of sample A. Grains large enough for their outline to be resolved are irregular and lumpy in shape (Figs. 11 and 12), suggesting they are aggregates rather than single crystals. The size distribution is shown in Fig. 13A. One very large grain (60 μm) observed in sample A (Fig. 12, location shown in Fig. 1A) is surrounded by a rim of carbonaceous matter in which a number of smaller Ni-P rich, as well as some apparent SiC grains (arrowed) are embedded. The oxygen content in this carbonaceous rim appears similar to that in the matrix.

EDS mapping and quantitative analysis of large grains show no visible zoning, although (Ni + Fe)/P atomic ratios obtained by microprobe WDS analysis vary from 4.3 to 5.7 with one outlier at 14.5 (Table 3). EDS analyses yield similar ratios. Average values obtained with the two methods are 5.60 ± 2.39 (WDS) and 5.69 ± 0.97 (EDS). From EDS mapping, Fe, S and O contents do not appear to differ strongly from those of the matrix (Fig. 11). Ni/Fe atomic ratios are high, ranging from 42 to 147 (average 79.2 ± 28.4, 1SD) for the WDS- and 28–114 (average 68.6 ± 29.5, 1SD) for the EDS data. In Fig. 14 element maps obtained by PIXE are shown for the region marked on Fig. 1A along with BSE and EDS oxygen abundance images in the same scale, and the outline of an area for which a quantitative analysis was carried out. Apart from P, Cu is the only element co-enriched with Ni, whereby the absolute Cu concentration is low (Table 4) such that it could not be detected by EDS or EMPA. The apparent Ni/Fe ratio is much lower than what we found using EMPA and SEM-EDS analyses, which is due to a general high Fe background generated by the surroundings of the grain, noting that PIXE analysis penetrates up to 100 μm below the sample surface (see Fig. 14; Al, Si and Ca values are also high, indicating the proximity of a fracture). However, the (Ni + Fe)/P ratio of 9.39 ± 0.34, higher than the averages of EMPA and SEM-EDS values, appears to be genuine and emphasizes the variable chemistry of this compound.

Phosphides common in iron meteorites are schreibersite and rhabdite, both $(Ni,Fe)_3P$, where schreibersite is the

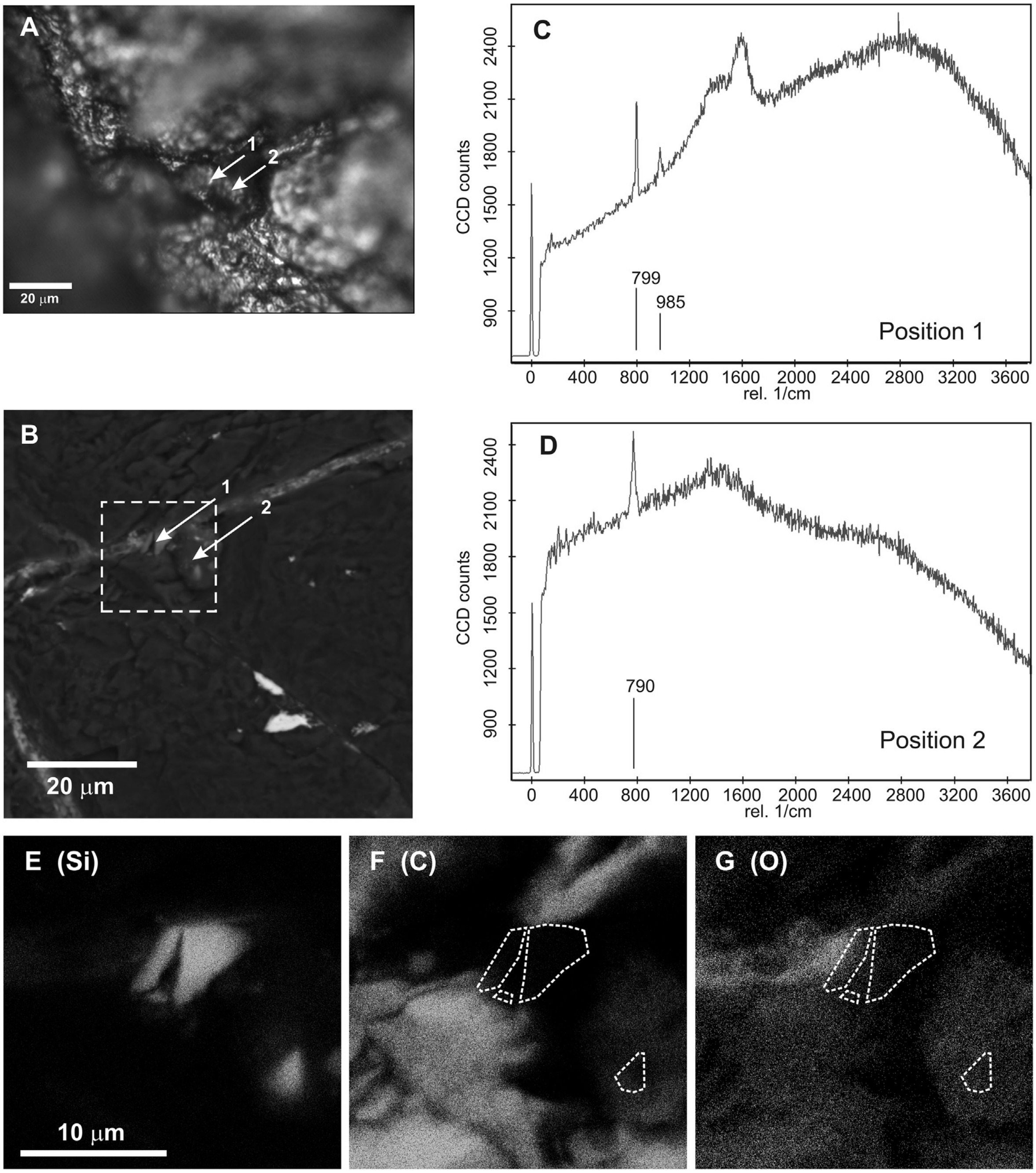

Fig. 10. occurrence and Raman spectra of silicon carbide, region 2 (circle with stippled outline) in Fig. 1A. **A and B:** optical and BSE images (the two BSE-bright grains in the lower half of B are Ni-phosphide, described further below). **C and D:** Raman spectra at localities 1 and 2 arrowed in A and B. Main SiC diagnostic band at 790–799 cm^{-1} as a single peak is indicative of cubic (β) SiC also found among large SiC grains from Murchison (Virag et al., 1992). The minor band at 985 cm^{-1} is not observed in all SiC. The high background is due to fluorescence, while C also shows minor, broad D and G bands (see Section 3.4). WITec Alpha 300R Raman microscope, excitation wavelength 532 nm, laser power 45 mW. **E, F, and G:** semiquantitative SEM-EDS element maps of square in B, for Si, C and O. Outlines of Si-rich grains transposed in C and O maps show low X-ray signals from C and O for these grains.

more Fe-rich variant (Geist et al., 2006). Further rare phosphides are $(Ni, Fe)_4P$, Melliniite from an acapulcoite (Pratesi et al., 2006) as well as the $(Ni, Fe)_2P$ phases barringerite (Buseck, 1969) and allabogdanite (Britvin et al., 2002) from pallasites and iron meteorites. Schreibersite and Barringerite have also been found in CM chondrites (Nazarov et al., 2009). The compound found in Hypatia is different from any reported ones in two respects: (1) it has much lower Fe than known varieties, and (2) it has higher (>5) and variable (Ni + Fe)/P atomic ratios (Fig. 15).

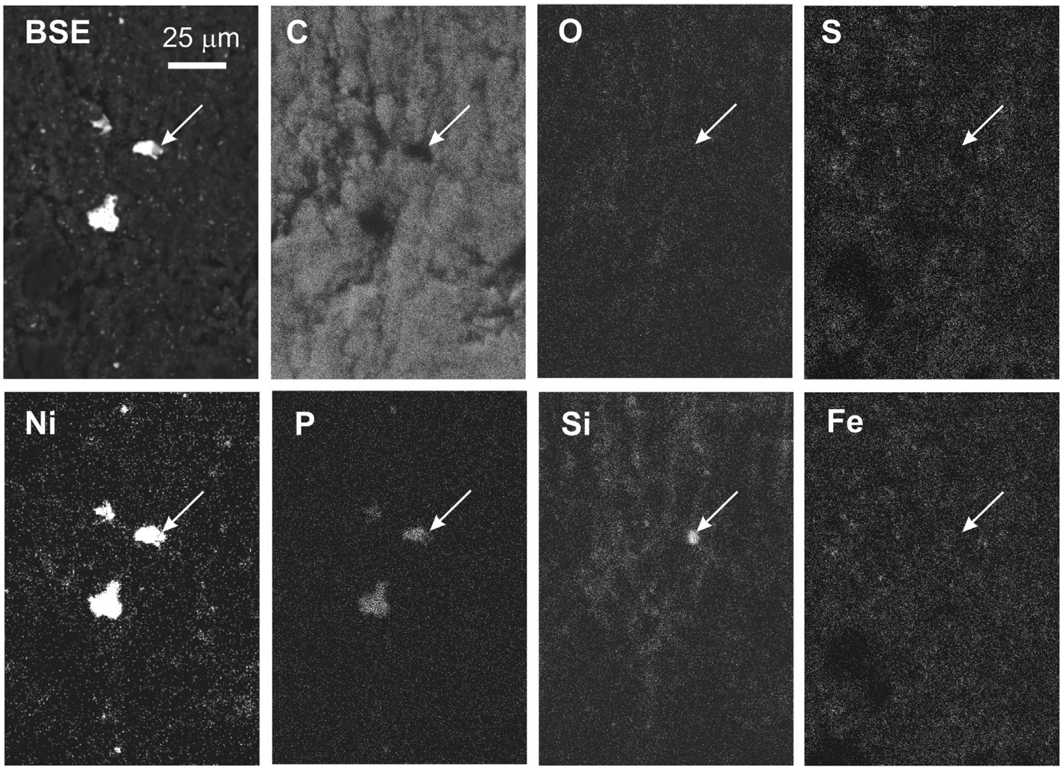

Fig. 11. BSE and selected EDS element maps of an area of sample A (indicated on Fig. 2) containing three 8–16 μm sized grains of Ni phosphide and a ca. 2 μm sized grain rich in silica, not associated with fractures (most probably SiC) and adjacent to one of the Ni-phosphide grains. Arrow pointing to the Si grain is replicated in the other frames to show relative BSE-brightness, absence of O and low C.

As the (Ni + Fe)/P ratios are both higher than those of any known phosphide mineral, and significantly variable, it appears likely that the Ni-phosphide observed is either an amorphous compound, or a cryptocrystalline mixture of a metal alloy and a phosphide. Given the high Ni/Fe ratio, any alloy component would be taenite. Similar to barringerite and schreibersite (RRUFF database, Lafuente et al., 2015), or any metallic alloy, the Ni-phosphide compound in Hypatia is Raman-inactive. It is optically highly reflective (Fig. 16) and has a greenish colour.

3.8. Association of Ni-phosphide and SiC

Fig. 11 shows two μm-sized Si-rich spots without noticeable O-enrichment, the larger of which is immediately adjacent to a Ni-phosphide grain. In both cases, the BSE-brightness of the Si-rich spots is only slightly elevated above that of Matrix-2, similar to the SiC grains identified by Raman spectroscopy. In Fig. 16, three larger such grains are seen, the largest of which, about 5 μm long, has a prismatic shape and appears in contact with a small Ni-phosphide cluster. In Fig. 12 five spots of high Si concentrations without significant O (arrowed) lie within the carbonaceous rim around the very large Ni-phosphide grain described above. The largest one is adjacent to a small Ni-phosphide grain. From their general similarity to the Raman-analyzed grains, we conclude that all these observed silicon-rich and oxygen-free grains are moissanite. The size distribution is shown in Fig. 13B. We note again that no carbide abrasives were used at any stage during our the sample preparation.

Compared to chondritic meteorites, both the high abundance of SiC and the occurrence of large grains of it in Hypatia are striking. Further, its frequent co-occurrence with the unique Ni-phosphide compound is remarkable.

3.9. Other, rare inclusions

Several types of inclusions were encountered only once. These include a rather large grain of metallic aluminium (Fig. 17A), and a phase consisting of silver, iodine and phosphorus (Fig. 17B and C). Further, small grains of metallic iron, silver and zinc in the 2–10 μm size range were found.

Apart from metallic Fe, such phases have not been reported from chondritic meteorites. The occurrence of a phase rich in iodine is interesting in the light of a marked ^{129}Xe anomaly observed by Avice et al. (2015), but absent in the grains studied by Kramers et al. (2013). ^{129}Xe is the daughter product of ^{129}I (half-life 15.7 Ma) which existed at the time of solar nebula formation (e.g. Brazzle et al., 1999). The ^{129}Xe anomaly is therefore proof of Hypatia's parent body being an early solar nebula object, and the occurrence of I in a rare, exotic grain suggests point sources of ^{129}Xe, thus accounting for the heterogeneous distribution of this isotope in Hypatia.

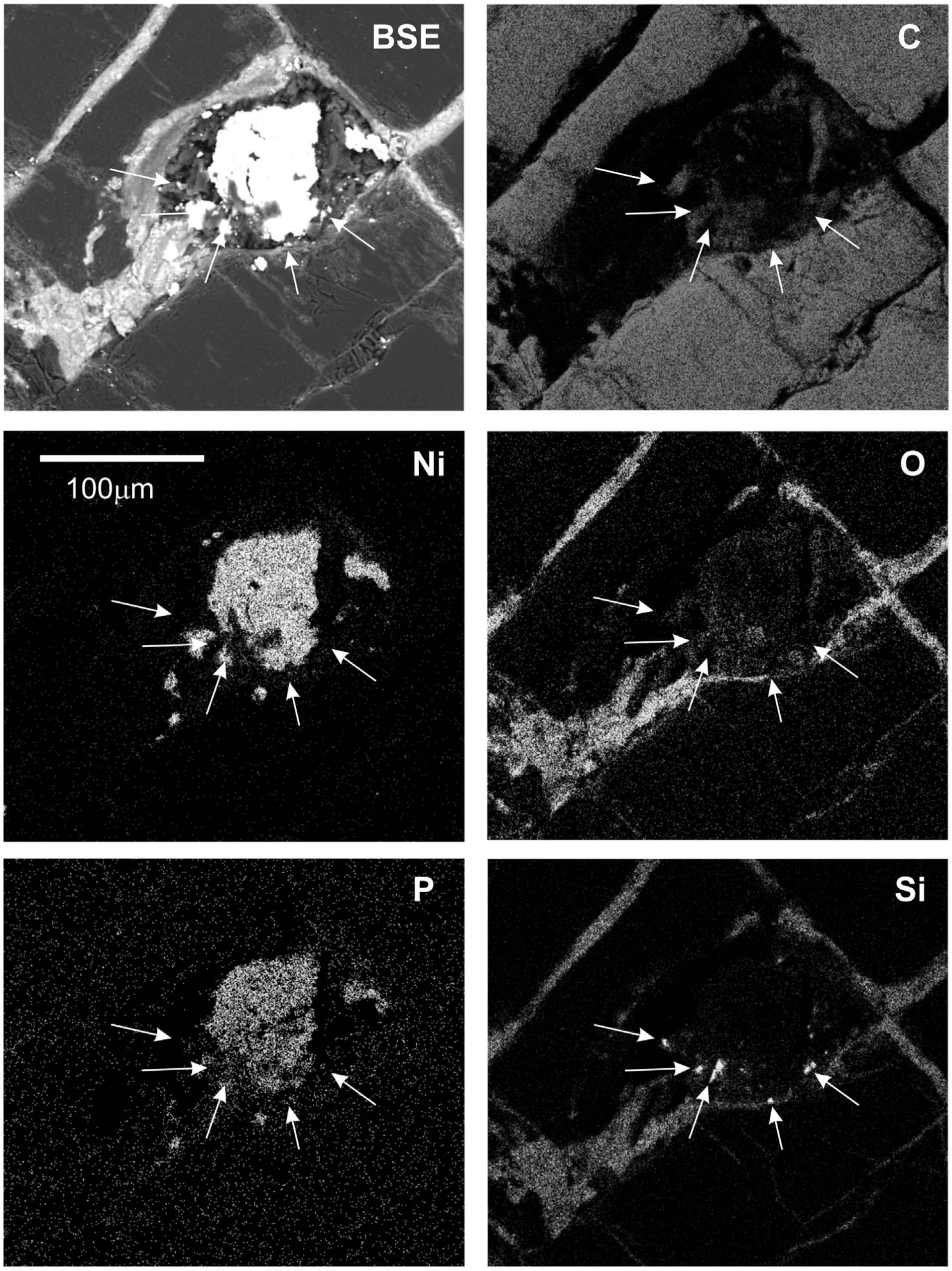

Fig. 12. Large irregular Ni phosphide grain marked in Fig. 1A, showing good coincidence of Ni and P, grainy rim of carbonaceous matter around the cluster and Si-rich, O-free grains (arrows, probably SiC) as well as small Ni-phosphide grains embedded in this.

4. DISCUSSION

4.1. Comparison with carbonado diamonds

It is of interest to revisit the comparison with carbonado diamonds (see introduction) in the light of the above observations. Carbonados are extremely hard, tough and cohesive polycrystalline diamond aggregates, consisting of partly interlocked grains ranging from ~0.5 to ~50 μm in size (Trueb and de Wys, 1969; De et al., 1998; Haggerty, 2014). They are mined from alluvial occurrences in Brazil and the Central African Republic, where they are derived from Proterozoic conglomerates. Specimens range from 0.05 to 20 g in mass with exceptional larger ones; the largest recorded being 633 g (Haggerty, 2014). They are invariably porous, with pores between 10 and 100 μm in size. These are in part filled by minerals of which orthoclase and hematite (and goethite) are the most common, while perovskite, zircon, rutile, allanite, gehlenite and REE phosphates also occur (Trueb and de Wys, 1969; De et al., 1998). These inclusions are suggestive of a strongly differentiated silicate magma. However, small inclusions of metals and alloys found enclosed in the diamond matrix, and moissanite actually intergrown with diamond, indicate an extremely

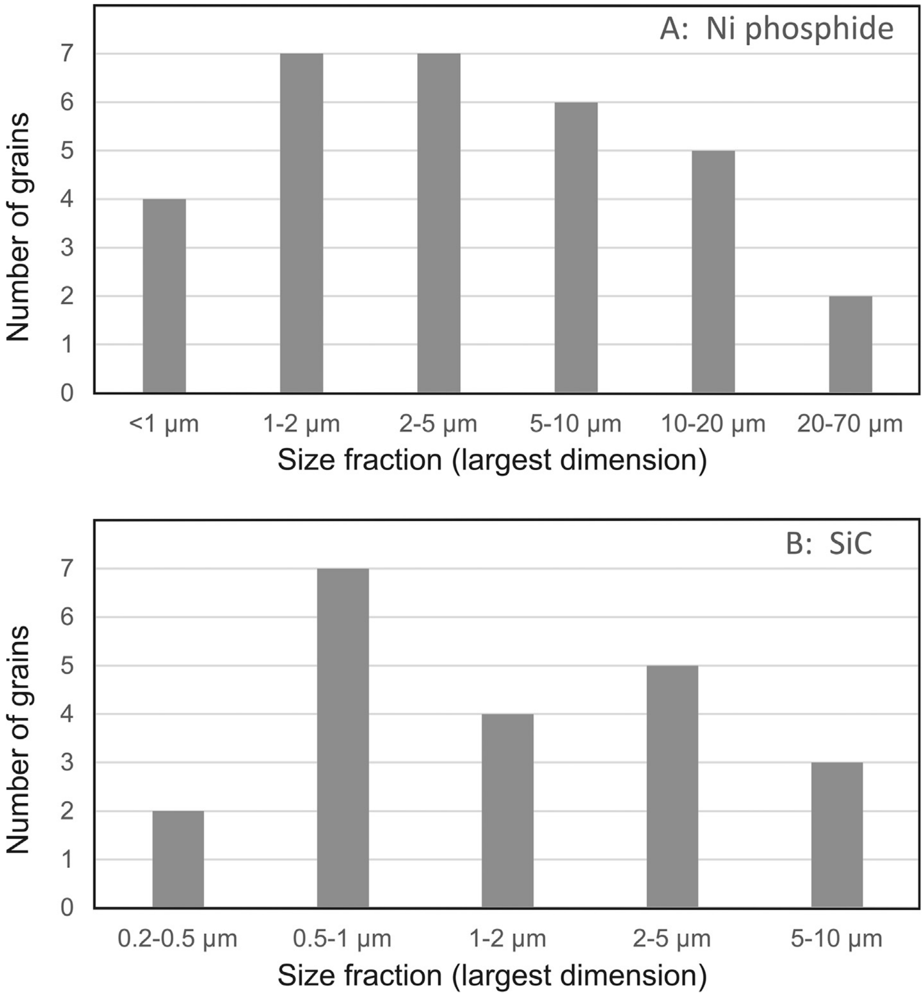

Fig. 13. Size distributions of **(A)** Ni phosphide and **(B)** silicon carbide grains found in Hypatia sample A. Note that SiC grains smaller than 0.2 µm are missed in SEM-EDS mapping of Si.

reducing environment of diamond crystallisation (De et al., 1998). Thus carbonados display strong chemical disequilibrium. The noble gas content of carbonados (including high temperature release) is terrestrial, with an additional important (but unsupported) ^{238}U-fission generated component found in Kr and Xe isotopes (Ozima et al., 1991). Unsupported radiogenic Pb and radiation-induced defects further indicate high uranium contents in the (probably Archean) geological past (Magee et al., 2016).

On a macroscopic scale, the extreme brittleness of the Hypatia stone, linked to its pervasive fracturing, sets it apart from carbonados. Further: (i) the individual diamond crystals in carbonados are larger by up to two orders of magnitude than those in Hypatia. (ii) No disordered carbon was detected in carbonados by Raman spectroscopy (Kagi and Fukura, 2008). (iii) Hypatia's matrix is not porous and does not contain silicate, phosphate or oxide minerals at all, let alone those typical of differentiated melts. (iv) The noble gas content in Hypatia is distinctly meteoritic and embodies no fissiogenic components, but instead shows a ^{129}Xe anomaly due to extinct ^{129}I (Avice et al., 2015). Thus, in addition to the contrast in carbon isotope ratios mentioned in the introduction, there is much evidence that the Hypatia stone cannot be a carbonado variety.

4.2. Comparison with extraterrestrial matter and the question of thermal processing

On the basis of C and N stable isotopes, the presence of diamonds, noble gas characteristics and a carbonaceous matrix, Avice et al. (2015) consider three types of meteoritic matter as having possibly a similar source to Hypatia. These are: graphite nodules in iron meteorites (cm-scale), nodules or veinlets in acapulcoites/lodranites (µm-scale), and carbonaceous matter occurring in ureilites as sub-mm-scale patches and veinlets. Avice et al. (2015) find that none of the three object types fully match the data from Hypatia. The data presented above can contribute to this discussion. Below we make some comparisons and attempt to find clues on the degree of pre-shock metamorphism undergone by Hypatia.

In iron meteorites, Fe sulphide (troilite) and graphite occur in intergrowths (often also including Fe carbides) that are mostly considered as a set of late magmatic

Table 3
Analytical data of nickel phosphide phase: EMPA and SEM-EDS data.

40 µm grain in Sample A, surface 1 (EMPA WDS, wt%)								Atomic ratios ± 1 SE (abs)	
			P	S	Fe	Ni	Sum	(Ni + Fe)/P	Ni/Fe
(detection limits)			(0.024)	(0.02)	(0.025)	(0.055)			
			10.07	n.d.	1.25	86.97	98.3	4.63 ± 0.21	66.2 ± 2.7
			9.69	n.d.	1.28	87.75	98.73	4.85 ± 0.22	65.2 ± 2.6
			8.46	n.d.	1.07	87.27	96.81	5.51 ± 0.25	77.6 ± 3.1
			9.1	0.02	1.29	89.02	99.42	5.24 ± 0.23	65.7 ± 2.7
			9.19	n.d.	0.58	89.09	98.86	5.15 ± 0.23	146.2 ± 5.9
			9.25	n.d.	1.06	87.48	97.81	5.05 ± 0.23	78.5 ± 3.2
			9.21	0.02	1.07	87.5	97.8	5.08 ± 0.23	77.8 ± 3.1
			10.22	n.d.	1.1	82.93	94.26	4.34 ± 0.19	71.7 ± 2.9
			7.8	n.d.	0.6	80.07	88.48	5.46 ± 0.24	127.0 ± 5.1
			9.77	n.d.	2	87.84	99.61	4.86 ± 0.22	41.8 ± 1.7
			9.61	n.d.	0.73	89.68	100.02	4.97 ± 0.22	116.9 ± 4.7
			8.47	n.d.	1.84	89.02	99.35	5.67 ± 0.25	46.0 ± 1.9
			2.97	0.03	1.38	80.01	84.39	14.5 ± 0.6	55.2 ± 2.2
			9.97	n.d.	1.25	87.48	98.7	4.70 ± 0.21	66.6 ± 2.7
			9.87	n.d.	1.12	89.68	100.67	4.86 ± 0.22	76.2 ± 3.1
			9.5	n.d.	0.92	85.75	96.17	4.82 ± 0.22	88.7 ± 3.6
					Average WDS ratios ± 1 SD			5.60 ± 2.39	79.2 ± 28.4
Large grain in Fig. 11 (EDS, wt%)									
	Al	Si	P		Fe	Ni	Sum		
	(0.03)	(0.05)	(0.05)		(0.06)	(0.6)	–		
	0.055	n.d.	9.15		0.74	88.89	98.88	5.17 ± 0.41	113.9 ± 6.9
	n.d.	0.088	8.85		0.87	88.82	98.64	5.35 ± 0.42	96.6 ± 5.9
	0.095	0.093	8.82		0.79	89.07	98.87	5.38 ± 0.42	106.9 ± 6.5
	0.090	0.177	9.06		0.96	88.30	98.58	5.20 ± 0.41	87.4 ± 5.3
	0.080	0.254	8.70		0.99	86.73	96.76	5.32 ± 0.42	83.3 ± 5.1
	0.104	0.155	8.58		0.96	89.10	98.9	5.54 ± 0.44	88.6 ± 5.4
	0.312	0.330	5.55		1.36	86.05	93.61	8.32 ± 0.66	60.0 ± 3.7
	0.104	0.334	7.24		1.18	85.62	94.47	6.33 ± 0.50	69.3 ± 4.2
3 grains in Fig. 2 (EDS, wt%)									
	n.d.	0.067	8.69		2.93	87.20	98.91	5.48 ± 0.43	28.3 ± 1.7
	0.144	0.196	8.13		1.98	86.47	96.93	5.75 ± 0.45	41.5 ± 2.5
	0.166	0.162	9.57		1.88	86.26	98.04	4.86 ± 0.38	43.6 ± 2.7
	0.108	0.056	7.19		2.54	88.71	98.6	6.71 ± 0.53	33.2 ± 2.0
	0.554	0.593	9.37		1.95	79.27	91.73	4.58 ± 0.36	38.7 ± 2.4
					Average EDS ratios ± 1SD			5.69 ± 0.97	68.6 ± 29.5
					Average all ratios ± 1SD			5.64 ± 1.86	74.4 ± 28.9

Detection limits in brackets.
Relative uncertainties (1 SE):
EMPA, P: 1.9% S: 60% Fe: 4% Ni: 0.6%.
SEM-EDS, Al: 30% Si: 20% P: 5% Fe: 6% Ni: 1.1%.

crystallisation or retrograde-metamorphic exsolution products accommodating excess sulphur in troilite, and excess carbon in carbides and graphite (Vdovykin, 1973; Scott and Goldstein, 2012). The nodules in which these assemblages occur can reach up to ca. 100 mm in diameter (Vdovykin, 1973). While troilite grains reach cm-size, individual graphite grains are usually smaller than 1 mm. Ni-phosphides occur associated with dominant kamacite and taenite in magmatic textures (Buseck, 1969; Britvin et al., 2002; Geist et al., 2006; Pratesi et al., 2006). Diamonds are rare and irregularly distributed in the graphite nodules, forming aggregates up to 5 mm consisting of µm-sized crystals; they are considered to be generated by the impact shock (Vdovykin, 1973). Acapulcoites and lodranites, although primitive, are igneous rocks (Cecchi and Caporali, 2015). In all these high temperature assemblages there are no reports of disordered carbon, contrasting with the ubiquitous presence of disordered carbon in the Hypatia matrix.

The comparison with ureilites is interesting. Silicate assemblages of these meteorites reflect igneous temperatures, resembling residues of extensive partial melting of material similar to CV chondrites (Goodrich, 1992, 2006). However, their oxygen isotopes are similar to the most primitive solar nebula matter (Clayton, 2003), and carbonaceous veins and patches, mostly not exceeding 0.5 mm in

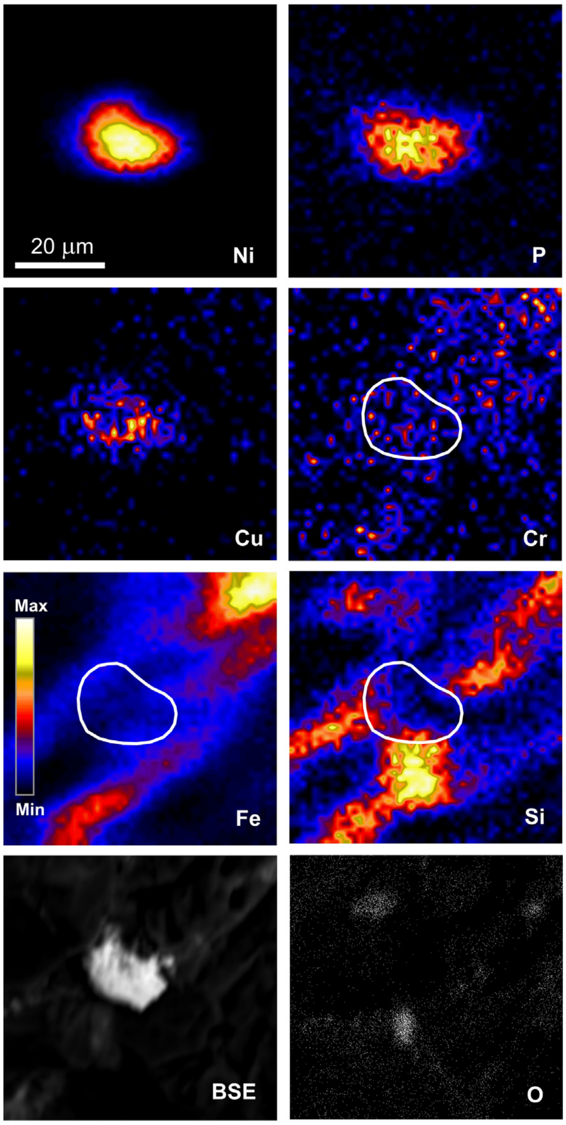

Fig. 14. PIXE non-quantitative element maps of region indicated in Fig. 1A, for Ni, P, Cu, Cr, Fe and Si, and BSE as well as EDS O images on the same scale. An analysis of the outlined area is given in Table 4.

size, have noble gas abundances similar to those of primitive carbonaceous chondrites (Goodrich, 1992; Avice et al., 2015). Ureilites are thus considered to have multiple sources (Goodrich, 1992; Rai et al., 2003a, 2003b). Avice et al. (2015) note similarities between Hypatia and ureilitic carbonaceous matter in both abundance patterns and isotope compositions of noble gases (Rai et al., 2003b), as well as in nitrogen isotopes, where Hypatia's high temperature release with $^{14}N/^{15}N \sim 0.00327$ ($\delta^{15}N \sim -110‰$) is identical to the value 0.00324 ± 0.00005 ($\delta^{15}N = -113 \pm 13‰$) for ureilitic diamonds (Rai et al., 2003a).

Table 4
PIXE analysis of area outlining a Ni, P rich inclusion, Fig. 14.

Element	Detection limit	Conc ± St. dev.
Ni (%)	0.0073	11.25 ± 0.11
Fe (%)	0.0028	0.893 ± 0.019
P (%)	0.011	0.633 ± 0.022
Si (%)	0.027	0.87 ± 0.11
Al (%)	0.152	1.06 ± 0.10
Sum		14.71
Ca (µg/g)	20	543 ± 38
Cu (µg/g)	89	423 ± 89
Ti (µg/g)	19	49 ± 10
S (µg/g)	60	<120
Cl (µg/g)	37	<75
K (µg/g)	24	<48
Mn (µg/g)	26	<52
Cr (µg/g)	20	<40
V (µg/g)	19	<37
Zn (µg/g)	53	<106
Atomic ratios		
Ni/P		9.39 ± 0.34
Ni/Fe		11.98 ± 0.28

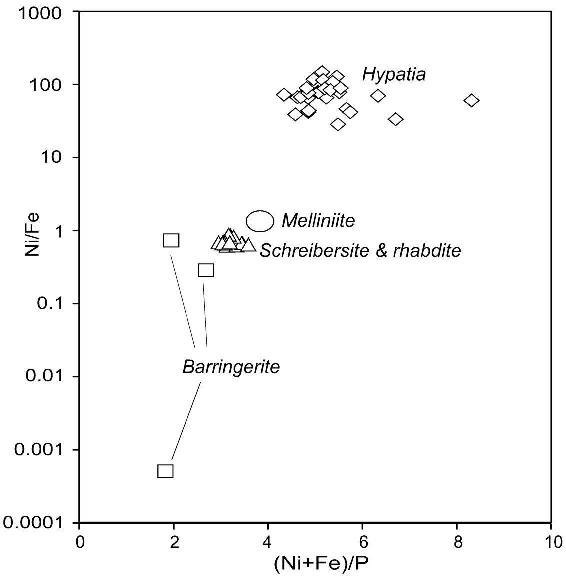

Fig. 15. Plot of Ni/Fe vs. (Ni + Fe)/P comparing phosphides found in this study with those described from pallasites and iron meteorites. Schreibersite and rhabdite: Geist et al. (2006). Melliniite: Pratesi et al. (2006) (ellipse gives range). Barringerite: Anthony et al. (2002).

Raman spectra of ureilite carbon reveal graphite (in some cases distorted), diamond coherent domains c. 40 nm in size (Le Guillou et al., 2010), diamond aggregates up to 40 µm in size (Jakubowski et al., 2011; Miyahara et al., 2015) and an ultra-hard intermediate phase (Ferroir et al. 2010). In the carbonaceous matter of the ureilite NWA 4742, a Raman study (Le Guillou et al., 2010) found graphite (well-ordered as well as distorted) as a dominant phase, in addition to diamond and disordered carbon with broad D and G bands and $I_D < I_G$. Using high resolution TEM, these authors could detect cases of diamond having been produced directly from graphite, and others where disordered carbon could either have been the precursor, or was produced by post-shock retrogression. Le Guillou et al. (2010) conclude that some ureilitic diamonds were

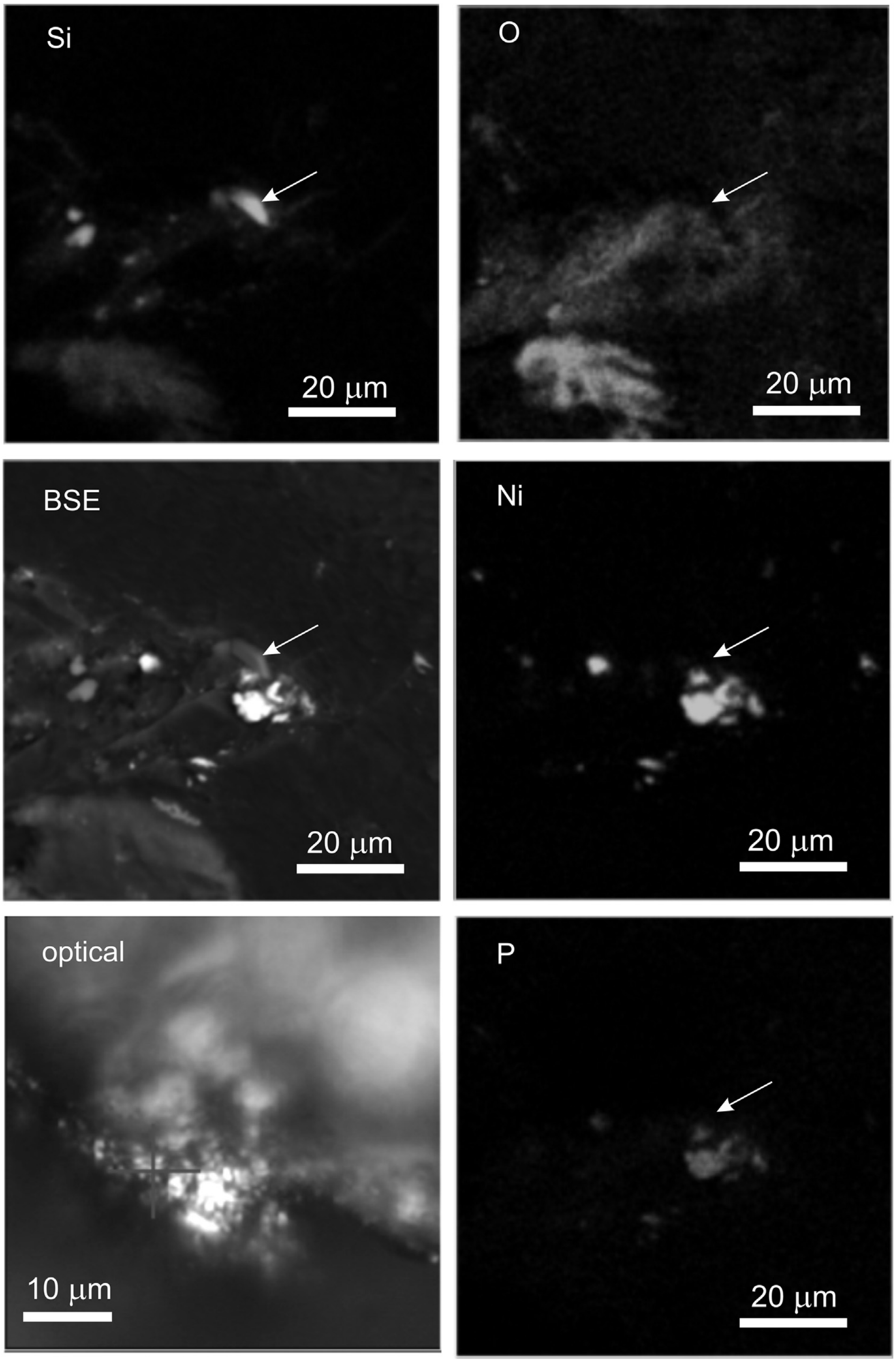

Fig. 16. BSE and optical images as well as EDS element maps of O, Si, Ni and P for an area in region 2 (circle with stippled outline) in Fig. 1A. O appears associated with minor cracks. Three SiC grains (rich in Si and containing no O are seen). One (arrowed), suggesting a prismatic habit, is adjacent to a Ni-phosphide grain. Reflected light image shows central portion of other images. The Ni-phosphide appears bright.

certainly formed by shock, but highlight the paradox presented by their high noble gas content (Matsuda et al., 1991, 1995; reinforced later by Rai et al., 2003b). In shock experiments yielding diamond from graphite, concentric onion-like carbon layers observed around diamonds were interpreted as post-shock retrogression products (Le Guillou et al., 2010). However, in contrast to the observations on NWA 4742, only distorted graphite, and no

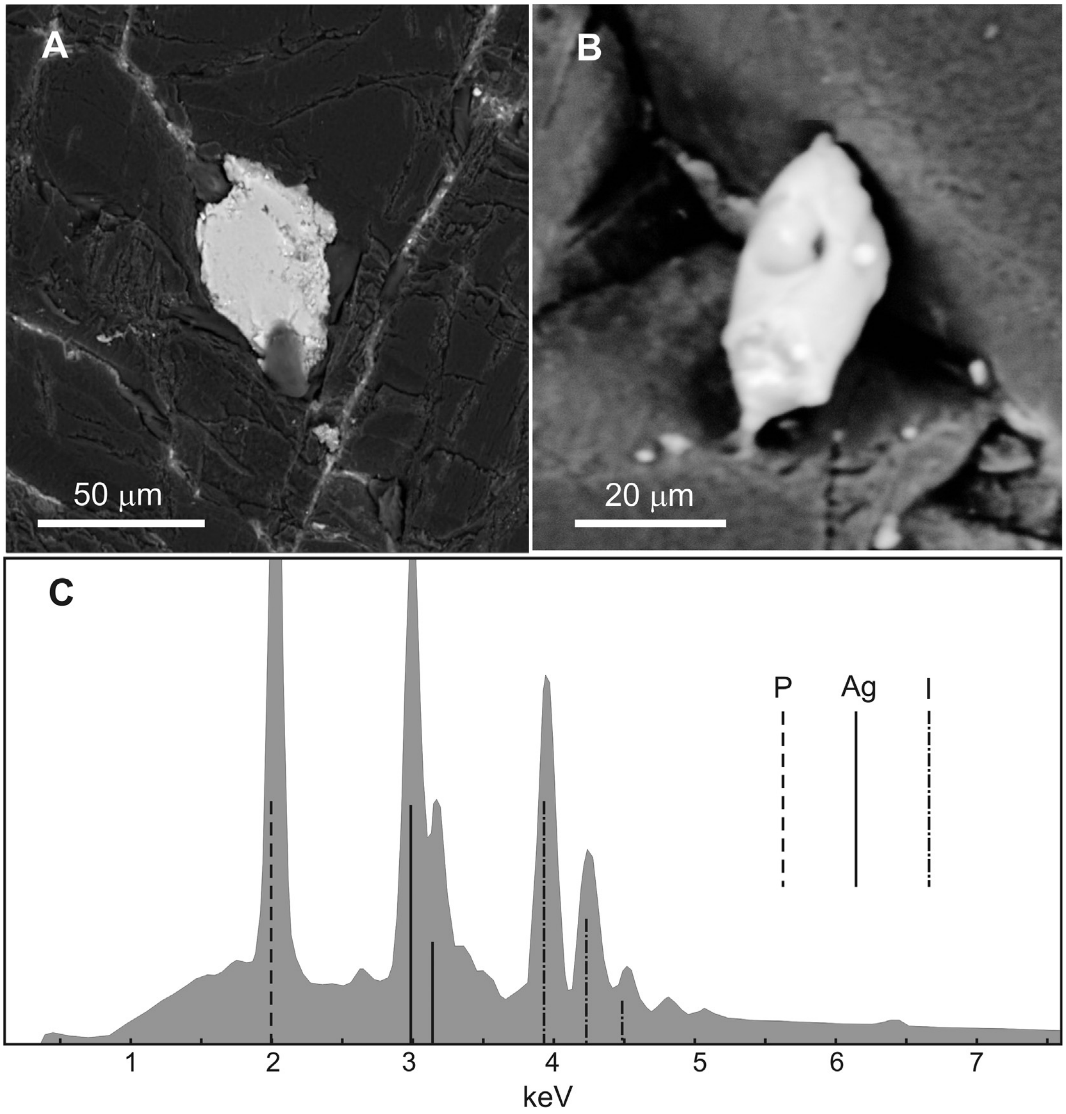

Fig. 17. two inclusion types found only once. **A:** native Al. **B:** phase consisting of Ag, P and I. **C:** EDS-spectrum for grain shown in (B).

disordered carbon similar to that in Hypatia, was found by Raman spectroscopy in their shock experiments. The possibility of originally disordered carbon coexisting, as a precursor, with shock-formed diamonds therefore remains for ureilites, and by analogy, in Hypatia. In summary, although ureilites are silicate-dominated rocks and their carbonaceous veinlets and patches are tiny, there are significant similarities between these and Hypatia.

As shown in Section 3.4 and Fig. 8A and B, types of extraterrestrial carbonaceous matter for which Raman spectra are comparable to the Hypatia matrix (disregarding the diamond content) are found in the most primitive carbonaceous chondrites (including Antarctic micrometeorites), in IDP's and in dust from Comet 81P/Wild. All these bodies contain abundant silicates. In carbonaceous Antarctic micrometeorites, silicates are dominant, as is true for all chondrites (Kurat et al., 1994). Further, the different types of IDP's (Bradley et al., 1988) and matter collected from comet 81P/Wild by NASA's Stardust mission (Zolensky et al., 2006) contain abundant and varied silicate grains, including GEMS (Glass with Embedded Metals and Sulphides) which are generally considered to be of interstellar origin (Bradley et al., 1999). In Antarctic micrometeorites (Yada et al., 2006) as well as in IDP's (Messenger et al., 2003; Floss et al., 2006) rare presolar silicate inclusions have been identified on the basis of isotopic anomalies. Nevertheless, it is worthwhile to compare petrographic and mineral data for the limited set of phases present in Hypatia with these other materials.

Regarding the Fe-Ni-S system, Ni-free grains of pyrrhotite up to 5 μm have been found in anhydrous IDP's, while hydrous ones yielded grains with variable Ni content, ranging to pentlandite composition (Zolensky and Thomas, 1995). In dust collected by NASA's Stardust mission from Comet 81P/Wild, Ni-free pyrrhotite grains, likewise up to 5 μm, as well as two pentlandite grains were identified (Zolensky et al., 2006). Carbonaceous micrometeorites (MM's) collected in Antarctic snow contain Fe-Ni sulphide grains up to 15 μm in size, with troilite being dominant and considered primary solar nebula dust, while minor pyrrhotite and rare pentlandite are suggested to be secondary products of hydrous alteration and atmospheric entry heating (Engrand et al., 2007; Dobrică et al., 2009). No specific association of these sulphides with organic matter is described for IDP's, MM's or Stardust. In primitive (CI and CM) carbonaceous chondrites, matrices have average (Fe + Ni)/S atomic ratios of 2.06 (CI, Palme and Jones, 2003) and 8.36 (CM, Zolensky et al., 1993), both of which are higher than the values we determined for Hypatia Matrix-2 (1.51 ± 0.24, Table 2). Fe-Ni sulphide as well as metal grains are common in the matrix of both CI and CM (Zolensky et al., 1993) and can reach up to 100 μm in size. With progressive thermal processing (from <200 to >600 °C) in the parent body of CM, the mineral association changes from pyrrhotite (Ni-bearing) + kamacite/martensite to pyrrhotite (with exsolution of pentlandite) + kamacite, to finally pyrrhotite (Ni-poor) + kamacite + taenite (Alexander et al., 1989; Kimura et al., 2011). Further, a mixed Ni-rich sulphide-phosphide phase, considered to be inherited from the hot Solar Nebula, appears to have exsolved P and Ni which were then accommodated in schreibersite and barringerite (Nazarov et al., 2009). These authors conclude that primary high temperature phases are preserved at low temperature, while exsolution occurs at medium temperatures and new equilibria are established only at high temperatures.

The sulphide-phosphide assemblage in Hypatia's Matrix-2 is very different from those outlined above. Pyrrhotite occurs in swarms of sub-μm grains in a carbon-dominated matrix with enhanced Fe and S concentrations, Fe/S > 1 and Ni/Fe < 0.1 (Figs. 2–5 and Table 2), without Ni-Fe metal or Fe carbide in the same assemblage. The Ni-phosphide compound with Ni/P > 5 and Ni/Fe ~ 75 occurs sporadically and haphazardly as grains or aggregates from <1 μm to >50 μm. Metallic Fe-Ni grains were not observed in Matrix-2 in this study, which can probably be understood from its much lower (Fe + Ni)/S ratio compared to the CM matrix.

While the Fe-Ni sulphides in Hypatia do not provide temperature information, some indications are given by the Ni-phosphide compound. In experimental studies on the Ni-Fe-P system, only the $(Ni, Fe)_3P$ phase has been produced. This is stable in equilibrium with Fe, Ni metals from the liquidus at c. 1000 °C down to 300 °C, the lowest temperature investigated, and can exist as a pure Ni end member (Doan and Goldstein, 1970; Romig and Goldstein, 1980). Given the very low solubility of P in taenite (<0.05 weight% below 500 °C, Romig and Goldstein, 1980), the Ni-rich compound in Hypatia should have exsolved a $(Ni, Fe)_3P$ phase, but in our EMPA or SEM EDS analyses and element maps, no such heterogeneity was observed. This suggests slow diffusion and reaction kinetics. Thermal annealing experiments on amorphous Ni-phosphide coatings produced by electrodeposition on a Cu-substrate (Bai and Hu, 2003) have shown that both internal annealing and two-way diffusivity of Cu and Ni are accelerated by increasing P content. At a P concentration of 17 at.% (close to the observed abundance in Hypatia's Ni-phosphide compound), after heating for 1 h at 200 °C, incipient Ni metal and Ni_3P diffraction lines were seen, and after heating at 300 °C these were well-defined. Extrapolation to the time scale of >1 Ma generally found for thermal metamorphism in chondrite parent bodies (Huss et al., 2006) implies that a crystalline internal structure with recognisable metallic and phosphide domains should have appeared in the Ni-phosphide compound (similar to the observations of Nazarov et al., 2009) if significant thermal processing had occurred. The conclusion that Hypatia underwent minimal or no pre-shock metamorphism is in accord with the results from our Raman study on Matrix-1 (Section 3.4).

4.3. Probable origins of mineral content

It has been argued above that, in Matrix-2, much of the Fe, and probably some S, reside in the carbonaceous matrix itself. This matrix has also been shown to be locally extremely enriched in trace elements such as Ir and Os (Fig. 1B and caption; see also Figs. 2 and 3 and Table 1 of Andreoli et al., 2015) without any visible mineralogical expression. The suggestion that the (Fe, Ni) sulphide phase crystallised from that matrix is tempting. At what stage in the history of the stone this would have occurred is a matter of speculation, but Hypatia's diamonds in the 0.2–1 μm size range are most probably formed by shock metamorphism (Kramers et al., 2013; Avice et al., 2015). A similar crystal size range also characterises the shock-related occurrence of the mineral bridgmanite ($MgSiO_3$ with perovskite structure) in the meteorite Tenham L6 (Tschauner et al., 2014). Thus, a sub-μm grain size can characterise minerals formed during shock events. On the basis of (i) the small grain size of the sulphide phase in Hypatia, (ii) the mineralogical context, which differs from that in chondrites, achondrites and irons, and (iii) the evidence (from diamond) for a shock event, we suggest that the Fe, Ni sulphide phase in Hypatia's Matrix-2 was formed in such an event within primary Fe- and S enriched domains. This hypothesis cannot be independently tested, but does not contradict any of the observations.

The coexistence of matrix types 1 and 2, two mainly carbonaceous but clearly distinguishable phases that are intimately intermingled, could indicate either unmixing of a previously single homogeneous substance, or mingling of two separate types of material, without mixing. Chemical contrasts help in addressing this question. The unmixing hypothesis requires the segregation of carbonaceous matter with several weight% metal content (possibly with sulphide minerals already formed) from a parent material, leaving an inclusion- and metal poor carbonaceous residue. We cannot envisage a process that could cause this type of segregation, and conclude that the two types of matrix must originally have been separate and were subsequently intermingled, presumably at the time of formation of Hypatia's parent body.

The most important inclusion types in the Hypatia matrix, other than pyrrhotite, are the Ni-phosphide compound and moissanite.

The Ni-phosphide compound reported here has not been described before, as it has higher Ni/P and vastly higher Ni/Fe ratios than known Ni-phosphide minerals (Fig. 15). While it was observed in both types of matrix, it is much more abundant in Matrix-2. Unlike the Fe sulphide, the Ni-phosphide grains do not occur in matrix regions enriched in their components and therefore cannot have crystallised from their matrix: they constitute extraneous matter. As such they could either be small fragments from a differentiated and subsequently destroyed precursor, or presolar grains. In the former case, dominant co-occurrence of taenite and/or kamacite as well as much lower Ni/Fe ratios would be expected, as all extraterrestrial (Ni, Fe) phosphides previously described occur as only minor constituents associated with these minerals, and have Ni/Fe ratios around unity or lower (Buseck, 1969; Britvin et al., 2002; Geist et al., 2006; Pratesi et al., 2006).

The high abundance of moissanite in the Hypatia Matrix-2 is reminiscent of some IDP's (Nguyen et al., 2007), although the grain size there is much smaller. Further, moissanite and other presolar minerals appear to be much rarer in material collected from comet 81P/Wild returned by NASA's Stardust mission (Brownlee et al., 2009). The apparently high proportion of rather large grains (Fig. 13B) is striking. In the >2 μm grains studied by Virag et al. (1992), the cubic symmetry coincided with low $^{12}C/^{13}C$ and high $^{14}N/^{15}N$ ratios characteristic of AGB stars, which also would provide a circumstellar environment with a potential for the high mass density needed to produce large grains (Virag et al., 1992 and references therein). However, such an origin for the moissanite grains in Hypatia remains speculative until *in situ* C and Si isotope measurements are carried out.

The general spatial association of moissanite with Ni-phosphide in Hypatia, with three observed cases of grains of the two phases actually occurring in contact with each other, suggests a common source. Since moissanite is known in meteorites only as a presolar mineral, a presolar origin for the Ni-phosphide compound is suggested by proxy. Metal alloys have not been described before as presolar matter, except as inclusions in graphite grains (Croat et al., 2003) and GEMS in IDP's (Floss et al., 2006) and 81P/Wild dust (Zolensky et al., 2006). This may not be surprising, as small alloy grains would probably be dissolved in the acid demineralizing processes commonly used to concentrate presolar minerals from meteorites.

Extrasolar grains are, with few exceptions (Virag et al., 1992; Zinner et al., 2011) very small (up to a few μm) as also predicted by theory (Salpeter, 1977), and the quite large Ni-phosphide grains (up to 60 μm) observed in the Hypatia stone appear in contradiction to this. However, as noted the shapes of these larger grains have very irregular morphologies suggesting they are aggregates, similar to the ca. 30 μm SiC grain described by Zinner et al. (2011). In particular the grain shown in Fig. 12, which is surrounded by smaller Ni-phosphide grains with moissanite grains in a granular rim of carbonaceous matter, has the appearance of an aggregate. Mantling of interstellar grains by refractory N and O bearing organic matter (CHON) is a well established phenomenon (Bradley, 1994; Bradley and Dai, 2004; Kimura et al., 2003), and the rim seen in Fig. 12 could be such a mantle. Any further discussion on the association of moissanite with the Ni-phosphide grains and the nature of a possible common origin should wait until *in situ* Ni, Si and C isotope data are available.

An origin as presolar grains also appears to be the most parsimonious explanation for the rare inclusions of metallic Al and Ag + P + I. Similar matter may be present in chondritic meteorites as well, but would (similar to Ni-phosphide) probably not have survived the acid treatment commonly used to concentrate IOM and presolar grains. The apparent ability of the Hypatia Matrix-2 precursor to collect and concentrate presolar grains is truly remarkable.

4.4. Possible causes of shock metamorphism

Observations on naturally shocked chondritic meteorites (Scott et al., 1992) as well as shock experiments on Murchison material (Tomeoka et al., 1999) reveal stark disequilibria. Melt veinlets are formed in matrix material still containing hydrous phyllosilicates. Only at extreme shock pressures (35 GPa and above) when the matrix is extensively melted, are these hydrous minerals eliminated from the experiments. The melts then contain vesicles, formed at the time of pressure release, that are the recipients of the volatiles from the broken down matrix minerals. Deformation of the matrix and flattening of chondrules occurs progressively between 10 and 20 GPa. From 20 to 30 GPa parallel 10–20 μm-spaced fracturing perpendicular to the axis of compression is seen. Above 30 GPa the orientation of fractures becomes more random and their spacing increases to around 50–100 μm. Fractures are open after decompression (Tomeoka et al., 1999). In collisions yielding shock pressures above c. 20 GPa, volatile content probably causes disintegration of carbonaceous chondrite matter during post-shock decompression (Tomeoka et al., 1999), which would explain the absence of highly-shocked carbonaceous chondrites (Scott et al., 1992).

Data for a comparison with Hypatia is very incomplete, because of the absence of silicates in Hypatia, and as melts could not develop in its carbonaceous matrix. However, the occurrence of disordered carbonaceous matter together with diamond in Hypatia is suggestive of disequilibrium conditions similar to the coexistence of hydrous phyllosilicates with melts in chondrites. Further, the pervasive, in part open fracturing with random orientation in Hypatia is reminiscent of the pattern seen in Murchison at shock pressures above 30 GPa (Tomeoka et al., 1999).

Shock metamorphism that affected the bolide containing the Hypatia stone, which we consider to have produced the diamonds, and presumably also the pyrrhotite, could have occurred either upon encounter with the Earth, or during an earlier impact in space. Kramers et al. (2013) argued for the former, mainly based on the occurrence of small inclusions of highly compressed atmospheric gases in mg-fractions of the stone, and these authors linked this with the suggestion of an airburst (Urey, 1957; Wasson, 2003; Boslough and Crawford, 2008). Modelling of high velocity atmospheric entry (Boslough and Crawford, 2008) reveals compression and flattening of the bolide (the so-called pancake model), which is ablated at the edges and disintegrates explosively while still transiting the atmosphere. The bulk of the released thermal energy is then primarily transported downward. It is thus possible for fragments to be thrown clear of the area subsequently covered by the fireball. Brief heating episodes do not necessarily cause chemical (or even isotopic) re-equilibration. For instance, in an LL6 chondrite clast embedded in the melt sheet of the ~144 Ma Morokweng impact crater, the $^{40}Ar/^{39}Ar$ signature of a 0.6 Ga collision in space was found to be preserved (Jourdan et al., 2010).

Very primitive carbonaceous bodies in the solar system are porous and usually hydrous. For comet nuclei, densities of c. 0.54–0.6 g/cm^3, corresponding to porosities of 65–75% have been determined (Asphaug and Benz, 1996; Jorda et al., 2016). Carbonaceous chondrites host water in hydrous silicates, while comets contain a variety of ices. A higher original porosity leads to more rapid deceleration in the atmosphere and therefore, for the same mass, higher pressure within the body prior to its disruption. Porosity appears not to affect fragmentation significantly, although larger fragments apparently correlate with greater porosity of the body (Benz and Jutzi, 2006; Jutzi et al., 2009).

Avice et al. (2015) concluded from the low abundance of cosmogenic ^{21}Ne and ^3He that Hypatia should either have been exposed to cosmic radiation in space for up to a maximum of c. 0.25 Ma, or was part of a bolide of at least several m in diameter. Meteoritic cosmic ray exposure ages less than 1 Ma are very rare (Eugster et al., 2006), whereas a large pre-shocked bolide is unlikely because a collision in space causing a shock pressure sufficient to generate diamonds in a volatile-rich carbonaceous body would have caused fragmentation as outlined above. Indications for the disintegration of a large, very unusual object above the area where Hypatia was found are provided by polymetallic (e.g. Ti, Al, Ag-metal) and carbonaceous (e.g. carbon nitride, PAHs and aliphatic hydrocarbons) debris in palaeosols from the Libyan Desert Glass area (Andreoli et al., 2017). From this perspective, the most parsimonious explanation for the shock features observed in the Hypatia stone would therefore be that it was delivered to Earth as part of a large bolide, which underwent shock and disintegration during atmosphere transit.

On the other hand, Avice et al. (2015) argue that the bimodal distribution of $^{15}N/^{14}N$ ratios, with ~0.00376 ($\delta^{15}N \sim +20‰$) being released at low temperatures, and ~0.00327 ($\delta^{15}N \sim -110‰$) at high temperatures (most probably from diamonds), would have been obliterated if these diamonds were formed by shock in atmosphere transit or terrestrial impact. This nitrogen isotope conundrum is akin to the noble gas problem of ureilitic diamonds (Matsuda et al., 1991, 1995; Rai et al., 2003b; Le Guillou et al., 2013; see Section 4.2). It applies to *in situ* diamond formation by shock, whether on Earth or in space, and remains a problem to be addressed.

4.5. The nature of the putative parent body

When considering what the parent body of Hypatia might have been, it is important to first realise that the matrix probably underwent degassing and must have been compressed, as well as probably deformed, during at least one shock episode.

The Hypatia stone is heterogeneous. Apart from the two types of matrix reported here, this is revealed by the noble gas abundances, for which the extraterrestrial component in the fragments analysed by Avice et al. (2015) was 5–10 times higher than those reported by Kramers et al. (2013), albeit with similar inter-element ratios. Also, the ^{129}Xe anomaly reported by Avice et al. (2015) was absent in the material analysed by Kramers et al. (2013). Further, Kramers et al. (2013) found some support for the presence of 'G' type Xe, Kr and Ne, which was only observed by Avice et al. (2015) in a single Ne analysis. This noble gas component is normally hosted in presolar SiC (Ott, 2002). Locally fairly abundant SiC grains that would be in accord with the presence of this component are inhomogeneously distributed even within the samples A and B studied here. The stone has been part of a large bolide (Avice et al., 2015), but in view of the heterogeneity seen, it need not be concluded that all of that bolide was of the same composition.

Hypatia is unique in combining a carbon-dominated chemistry, absence of silicates, depletion in lithophile elements, *in situ* observation of large SiC grains and a previously unreported Ni phosphide compound. A lack of pre-shock thermal processing is indicated by the Raman D-G band characteristics of the carbonaceous matrix (disregarding the ubiquitous diamond sp^3 band), as well as by the Ni phosphide not showing any recrystallization. This inferred lack of significant thermal processing is reminiscent of the cold agglomeration demonstrated for the least equilibrated carbonaceous chondrites (Buseck and Hua, 1993) or the parent bodies of cluster IDP's that preserve molecular cloud material (Messenger, 2000).

The average Ni/Fe ratio of Matrix-2 (0.086 ± 0.061) overlaps both solar and CI values (0.055 and 0.063, respectively). The average (Ni + Fe)/S ratio found in Matrix-2 (1.51 ± 0.24) is consistent with the solar ratio (1.40) but lower than the CI value (2.06) (Table 2; Palme and Jones, 2003; the difference between solar and CI values is due to the volatility of S). Here, however, the chemical similarity between Hypatia and CI or solar compositions ends, as all lithophile elements are strongly depleted in the Hypatia stone, as would be expected due to the absence of silicates. Further, the extreme enrichment of certain platinum group elements in 20–100 μm domains as reported by Andreoli et al. (2015) bears no similarity to any known meteorite material. Labelling the stone as an object of cometary origin, as originally suggested by Kramers et al. (2013) would be in accord with its apparently unprocessed character. However, all cometary matter studied in the laboratory so far (IDP's and dust from 81P/Wild, Bradley et al., 1988; Messenger et al., 2003; Floss et al., 2006; Zolensky et al., 2006) and by high resolution spectroscopy (Wooden, 2002) contains silicate grains, mainly GEMS, which have not been found in Hypatia. Also, carbonaceous matrix rich in Fe, Ni, S and P has not been observed in IDP's and 81P/Wild dust. The latter may be very difficult to detect if only minuscule grains are available for study, but the former is a solid observation. If the Hypatia stone is a comet fragment, it seems to belong to a class different from known cometary matter.

Unless a process exists that could have separated carbonaceous from silicate dust in interstellar space or in the accreting nebula, it must be concluded that the absence of silicates in Hypatia reflects gross heterogeneity of matter accreting in the early solar nebula, particularly with respect to the abundance of silicate matter. *In situ* stable isotope work on Hypatia's matrix is crucial to further constrain hypotheses about the parent body of this enigmatic object.

5. CONCLUSIONS

The Hypatia stone is pervasively fractured, and these fractures contain silicate, carbonate and oxide matter that is unrelated to its carbonaceous matrix. At even small (about 10 μm) distances from these fractures, the carbonaceous matrix of the Hypatia stone is unaltered.

Two types of matrix were identified: Matrix-1, consisting essentially of pure carbonaceous matter, and Matrix-2, which contains Fe, Ni, P and S in concentrations detectable by SEM EDS and quantifiable by EMPA. In Matrix-2, inclusions of pyrrhotite up to 1 μm occur, although measured element ratios (Fe excess over S) indicate that a significant proportion of Fe, and possibly also S, is housed in the carbonaceous matrix. The mode of occurrence of the pyrrhotite grains suggests they were shock generated.

Other minerals identified are: (1), graphite, in a cluster of grains up to about 10 μm, occurring in Matrix-2; (2) moissanite, in grains up to 5 μm, occasionally with apparent crystalline habit, only seen in Matrix-2 and associated with (3), a Ni-phosphide compound with variable atomic Ni/P ratios >5, in up to 60 μm aggregates of apparently cryptocrystalline or amorphous matter, that occurs in both matrix types but is much more common in Matrix-2; (4) a large (50 μm) grain of metallic aluminium, in Matrix-2; (5) a single 15 μm grain containing Ag, I and P, in Matrix-2. Moissanite and the Ni-phosphide compound are thought to be presolar, while a presolar origin of graphite, metallic Al and the Ag-I compound is also considered possible.

Raman spectroscopy shows that diamond is present in both Matrix-1 and Matrix-2, but appears more prevalent in Matrix-2. In Matrix-1, the D and G bands of disordered carbon are evident, and their FWHM as well as the D/G intensity ratio are similar to those of the most primitive meteoritic, as well as cometary carbonaceous matter. From this observation, and the apparently not annealed nature of the Ni-phosphide compound, we consider that Hypatia did not undergo thermal processing over a million year time scale. Shock metamorphism probably occurred upon encounter with the Earth.

The Hypatia stone differs from known primitive solar system objects in that it is carbon-dominated and apparently devoid of silicates, even GEMS. Following our hypothesis of an extraterrestrial origin, this could point to strong heterogeneity in the early solar nebula (and possibly interstellar clouds) with respect to silicate content. *In-situ* stable isotope studies of the carbonaceous matrix as well as C, Si and Ni isotope analyses on moissanite and the Ni-phosphide phase, respectively, will help to settle the debate on the nature of Hypatia's parent matter, could provide crucial clues to the origin of its components, and may possibly shed new light on aspects of the early solar nebula.

ACKNOWLEDGEMENTS

Ilona Schäpan and Christian Reinke are thanked for their help with the SEM EDS analyses at Helmholtz Zentrum Potsdam, and with the EMPA WDS analyses at UJ, respectively. Rainer Wieler provided constructive comments on an earlier version of the manuscript. GAB's research fellowship is funded by the UJ University Research Council (PPM research Centre). JDK gratefully acknowledges SA NRF incentive funding for rated researchers. The WITec Raman instrumentation at UJ was donated by Assore Ltd. Insightful reviews by Eric Quirico and three anonymous referees on an earlier version of the manuscript are gratefully acknowledged.

REFERENCES

Alexander C. M. O'D., Barber D. J. and Hutchinson R. H. (1989) The microstructure of Semarkona and Bishunpur. *Geochim. Cosmochim. Acta* **53**, 3045–3057.

Allamandola L. J., Sandford S. A. and Wopenka B. (1987) Interstellar polycyclic aromatic hydrocarbons and carbon in interplanetary dust particles and meteorites. *Science* **237**, 56–59.

Anders E. and Zinner E. (1993) Interstellar grains in primitive meteorites – diamond, silicon carbide, and graphite. *Meteoritics* **28**, 490–514.

Andreoli, M. A. G., Di Martino, M., Pischedda, V., Gibson, R. L., Huotari, S., Kallonen, A., Belyanin, G., Erasmus, R., Ziegler, A., Mouri, H., Ntsoane, T., van der Merwe, R., Lekgoathi, M. D. S., Jinnah, Z., Kramers, J., Serra, R., Sighinolfi, G. P., Stengel, I., Kock, L. D., Block, D., Chawn, L., Bamford, M., Rumbold, K. and Billing, D. (2017) Polymetallic and carbonaceous debris in palaeosol from the Libyan Desert Glass Strewnfield, S Egypt: evidence of a cometary impact. In: Lunar and Planetary Science XLVIII. Lunar Planet. Inst., Houston. #1045 (abstr.).

Andreoli M. A. G., Przybylowicz W. J., Kramers J., Belyanin G., Westraadt J., Bamford M., Mesjasz-Przybylowicz J. and Venter A. (2015) PIXE micro-mapping of minor elements in Hypatia, a diamond bearing carbonaceous stone from the Libyan Desert Glass area, Egypt: Inheritance from a cold molecular cloud? *Nucl. Instr. Methods Phys. Res. B* **363**, 79–85.

Anthony, J. W., Bideaux, R. A., Bladh, K. W. and Nichols, M. C. (eds.) (2002) *Handbook of Mineralogy*. Mineralogical Society of America, Chantilly, VA 20151-1110, USA, <http://www.handbookofmineralogy.org/>.

Arpigny C., Jehin E., Manfroid J., Hutsemékers D., Schulz R., Stüwe J. A., Zucconi J. M. and Ilyin I. (2003) Anomalous nitrogen isotope ratio in comets. *Science* **301**, 1522–1524.

Asphaug E. and Benz W. (1996) Size, density, and structure of comet Shoemaker-Levy 9 inferred from the physics of tidal breakup. *Icarus* **121**, 225–248.

Avice G., Meier M. M. M., Marty B., Wieler R., Kramers J. D., Langenhorst F., Cartigny P., Maden C., Zimmermann L. and Andreoli M. A. G. (2015) A comprehensive study of noble gases and nitrogen in "Hypatia", a diamond-rich pebble from SW Egypt. *Earth Planet. Sci. Lett.* **432**, 243–253.

Bai A. and Hu C.-C. (2003) Effects of annealing temperatures on the physicochemical properties of nickel–phosphorus deposits. *Mater. Chem. Phys.* **79**, 49–57.

Barakat A. A. (2012) *The Precious Gift of Meteorites and Meteorite Impact Processes*. Nova Sciences Publishers Inc, New York, p. 166.

Benz, W. and Jutzi, M. (2006) Collision and impact simulations including Porosity. In: Milani, A., Valsecchi, G. B. and Vokrouhlický, D. (Eds.), Near Earth Objects, our Celestial Neighbors: Opportunity and Risk. Proceedings International Astronomical Union Symposium, vol. 236, pp. 223–232, doi: http://doi.org/10.1017/S1743921307003262.

Beyssac O., Goffé B., Petitet J.-P., Froigneux E., Moreau M. and Rouzaud J.-N. (2003) On the characterization of disordered and heterogeneous carbonaceous materials by Raman spectroscopy. *Spectrochim. Acta A* **59**, 2267–2276.

Bland, P. A., Zolensky, M. E., Benedix, G. K. and Sephton, M. A. (2006) Weathering of Chondritic Meteorites. In: Lauretta, D. S., McSween, H. Y. (Eds.), Meteorites and the Early Solar System II. Univ. Arizona Press, Tucson, AZ, pp. 852–867.

Bockelée-Morvan D., Biver N., Jehin E., Cochran A. L., Wiesemeyer H., Manfroid D., Hutsemékers D., Arpigny C., Boissiers J., Cochran W., Colom P., Crovisier J., Milutinovic N., Moreno R., Prochaska J. X., Ramirez I., Schulz R. and Zucconi J.-M. (2008) Large excess of heavy nitrogen in both nitrogen cyanide and cyanogen from Comet 17P/Holmes. *Astrophys. J.* **679**, L49–L52.

Bonal L., Bourot-Denise M., Quirico E., Montagnac G. and Lewin E. (2007) Organic matter and metamorphic history of CO chondrites. *Geochim. Cosmochim. Acta* **71**, 1605–1623.

Bonal L., Quirico E., Bourot-Denise M. and Montagnac G. (2006) Determination of the petrologic type of CV3 chondrites by Raman spectroscopy of included organic matter. *Geochim. Cosmochim. Acta* **70**, 1849–1863.

Bonal, L., Quirico, E., Montagnac, G. and Reynard, B. (2005) Laser-induced fluorescence: potential interests for immature organic matter characterization. In: Lunar Planet. Sci. XXXVI Lunar Planet. Inst., Houston. #1858(abstr.).

Bonal L., Quirico E., Flandinet L. and Montagnac G. (2016) Thermal history of type 3 chondrites from the Antarctic meteorite collection determined by Raman spectroscopy of their polyaromatic carbonaceous matter. *Geochim. Cosmochim. Acta* **189**, 312–337.

Boslough M. B. E. and Crawford D. A. (2008) Low-altitude airbursts and the impact threat. *Int. J. Impact Eng.* **35**, 1441–1448.

Bradley J. P. (1994) Chemically anomalous preaccretionally irradiated grains in interplanetary dust from comets. *Science* **265**, 925–929.

Bradley J. P. and Dai Z. R. (2004) Mechanism of formation of glass with embedded metal and sulphides. *Astrophys. J.* **617**, 650–655.

Bradley J. P., Keller L. P., Snow T. P., Hanner M. S., Flynn G. J., Gezo J. C., Clemett S. J., Brownlee D. E. and Bowey J. E. (1999) An infrared spectral match between GEMS and interstellar grains. *Science* **285**, 1716–1718.

Bradley J. P., Sandford S. A. and Walker R. M. (1988) Interplanetary dust particles. In *Meteorites and the Early Solar System* (eds. J. F. Kerridge and M. S. Matthews). Univ. Arizona Press, Tucson, AZ, pp. 861–895.

Brazzle R. H., Pravdivtseva O. V., Meshik A. P. and Hohenberg (1999) Verification and interpretation of the I-Xe chronometer. *Geochim. Cosmochim. Acta* **62**, 739–760.

Britvin S. N., Rudashevsky N. S., Krivovichev S. V., Burns P. C. and Polekhovsky Y. S. (2002) Allabogdanite, (Fe, Ni)2P, a new mineral from the Onello meteorite: the occurrence and crystal structure. *Am. Mineral.* **87**, 1245–1249.

Brownlee, D. E., Joswiak, D., Matrajt, G., Messenger, S. and Ito, M. (2009) Silicon carbide in comet Wild 2 & the abundance of pre-solar grains in the Kuiper Belt. In: Proceedings of the 40th Lunar & Planetary Science Conference, p. 2195.

Buseck P. R. (1969) Phosphide from meteorites: barringerite, a new iron-nickel mineral. *Science* **165**, 169–171.

Buseck P. R. and Hua X. (1993) Matrices of carbonaceous chondrite meteorites. *Annu. Rev. Earth Planet. Sci.* **21**, 255–305.

Busemann H., Baur H. and Wieler R. (2000) Primordial noble gases in "phase Q" in carbonaceous and ordinary chondrites studied by closed-system stepped etching. *Meteorit. Planet. Sci.* **35**, 949–973.

Busemann H., Alexander C. M. O'D. and Nittler L. R. (2007) Characterization of insoluble organic matter in primitive meteorites by microRaman spectroscopy. *Meteorit. Planet. Sci.* **42**, 1387–1416.

Busemann H., Nguyen A. N., Cody G. D., Hoppe P., Kilcoyne A. L. D., Stroud R. M., Zega T. J. and Nittler L. R. (2009) Ultra-primitive interplanetary dust particles from the comet 26P/Grigg–Skjellerup dust stream collection. *Earth Planet. Sci. Lett.* **288**, 44–57.

Cartigny P. and Marty B. (2013) Nitrogen isotopes and mantle geodynamics: the emergence of life and the atmosphere–crust–mantle connection. *Elements* **9**, 359–366.

Cecchi V. M. and Caporali S. (2015) Petrologic and minerochemical trends of acapulcoites, winonaites and lodranites: new evidence from image analysis and EMPA investigations. *Geosciences* **5**, 222–242. https://doi.org/10.3390/geosciences5030222.

Clayton R. N. (2003) Oxygen isotopes in the solar system. *Space Sci. Rev.* **106**, 19–32.

Croat T. K., Bernatowicz T., Amari S., Messenger S. and Stadermann F. J. (2003) Structural, chemical, and isotopic microanalytical investigations of graphite from supernovae. *Geochim. Cosmochim. Acta* **67**, 4705–4725.

Davidson J., Busemann H., Nittler L. R., Alexander C. M. O'D. and Orthous-Daunay F.-R. (2014) Abundances of presolar silicon carbide grains in primitive meteorites determined by NanoSIMS. *Geochim. Cosmochim. Acta* **139**, 248–266.

Doan A. S. and Goldstein J. I. (1970) The ternary phase diagram, Fe-Ni-P. *Metall. Trans.* **1**, 1759–1767.

De S., Heaney P. J., Hargraves R. B., Vicenzi E. P. and Taylor P. T. (1998) Microstructural observations of polycrystalline diamond: a contribution to the carbonado conundrum. *Earth Planet. Sci. Lett.* **164**, 421–433.

De S., Heaney P. J., Vicenzi E. P. and Wang J. (2001) Chemical heterogeneity in carbonado, an enigmatic polycrystalline diamond. *Earth Planet. Sci. Lett.* **185**, 315–330.

Dobrică E., Engrand C., Duprat J., Gounelle M., Leroux H., Quirico E. and Rouzaud J.-N. (2009) Connection between micrometeorites and Wild 2 particles: from Antarctic snow to cometary ices. *Meteorit. Planet. Sci.* **44**, 1643–1661.

Dobrică E., Engrand C., Quirico E., Montagnac G. and Duprat J. (2011) Raman characterization of carbonaceous matter in CONCORDIA Antarctic micrometeorites. *Meteorit. Planet. Sci.* **46**, 1363–1375.

Engrand, C., Duprat, J., Maurette, M., and Gounelle, M. (2007) Fe-Ni sulphides in CONCORDIA Antarctic micrometeorites. In: Lunar Planetary Science XXXVIII. Lunar Planet. Inst., Houston. #1668(abst.).

Eugster, O., Herzog, G. F., Marti, K. and Caffee, M. W. (2006) Irradiation records, cosmic-ray exposure ages, and transfer times of meteorites. In Meteorites and the Early Solar System II (eds. D. S. Lauretta and H. Y. McSween). Univ. Arizona Press, Tucson, AZ, pp. 829–851.

Ferroir T., Dubrovinsky L., El Goresy A., Simionovici A., Nakamura T. and Gillet P. (2010) Carbon polymorphism in shocked meteorites: Evidence for new natural ultrahard phases. *Earth Planet. Sci. Lett* **290**, 150–154.

Floss C. and Stadermann F. J. (2009) High abundances of circumstellar and interstellar C-anomalous phases in the primitive CR3 chondrites QUE 99177 and MET 00426. *Astrophys. J.* **697**, 1242–1255.

Floss C., Stadermann F. J., Bradley J. P., Dai Z. R., Bajt S., Graham G. and Lea A. S. (2006) Identification of isotopically primitive interplanetary dust particles: a NanoSIMS isotopic imaging study. *Geochim. Cosmochim. Acta* **70**, 2371–2399.

Füri E. and Marty B. (2015) Nitrogen isotope variations in the Solar System. *Nat. Geosci.* **8**, 515–522. https://doi.org/10.1038/ngeo2451.

Geist V., Wagner G., Nolze G. and Moretzki O. (2006) Investigations of the meteoritic mineral (Fe, Ni)3P. *Cryst. Res. Technol.* **40**, 52–64.

Goodrich C. A. (1992) Ureilites: a critical review. *Meteoritics* **27**, 327–352.

Goodrich, C. A. (2006) Composition of ureilite precursor materials. In Proceedings of the Lunar & Planetary Science XXXVII. Lunar Planet. Inst., Houston. #1194(abstr.).

Grady M. M. and Wright I. P. (2003) Elemental and isotopic abundances of carbon and nitrogen in meteorites. *Space Sci. Rev.* **106**, 231–248.

Haenecour, P., Floss, C., Wang, A., Gyngard, F., Amari, S. and Jadhav, M. (2015) A unique presolar graphite in the CO3.0 chondrite LAP 031117. In: Proceedings of the Lunar & Planetary Science XLVI. Lunar Planet. Inst., Houston. #5006 (abstr.).

Haggerty S. E. (2014) Carbonado: physical and chemical properties, a critical evaluation of proposed origins, and a revised genetic model. *Earth. Sci. Rev.* **130**, 49–72.

Henke B. L. (1964) X-ray fluorescence analysis for sodium, fluorine, oxygen, nitrogen, carbon and boron. *Adv. X-Ray Anal.* **7**, 460–488.

Henke B. L. and Tester M. A. (1975) Techniques of low-energy X-ray spectroscopy (0.1–2 keV region). *Adv. X-Ray Anal.* **18**, 76–106.

Huss G. R. and Lewis R. S. (1995) Presolar diamond, SiC and graphite in primitive chondrites. *Geochim. Cosmochim. Acta* **59**, 115–160.

Huss G. R., Meshik A. P., Smith J. B. and Hohenberg C. M. (2003) Presolar diamond, silicon carbide, and graphite in carbonaceous chondrites: implications for thermal processing in the solar nebula. *Geochim. Cosmochim. Acta* **67**, 4823–4848.

Huss, G. R., Rubin, A. E. and Grossman, J. N. (2006) Thermal metamorphism in chondrites. In Meteorites and the Early Solar System II (eds. D. S. Lauretta, H. Y. McSween). Univ. Arizona Press, Tucson, AZ, pp. 567–586.

Jakubowski T., Karczemska A. and Kozanecki M. (2011) Diamonds in ureilites. *Meteorites*, 3–8.

Jewitt D. C., Matthews H. E., Owen T. and Meier R. (1997) Measurements of $^{12}C/^{13}C$, $^{14}N/^{15}N$, and $^{32}S/^{34}S$ Ratios in Comet Hale-Bopp (C/1995 01). *Science* **278**, 90–93.

Jorda L., Gaskell R., Capanna C., Hviid S., Lamy P., Ďurech J., Faury G. O., Groussin G. O., Gutiérrez P., Jackman C., Keihm S. J., Keller H. U., Knollenberg J., Kührt E., Marchi S., Mottola S., Palmer E., Schloerb F. P., Sierks H., Vincent J.-B., A'Hearn M. F., Barbieri C., Rodrigo R., Koschny D., Rickman H., Barucci M. A., Bertaux J. L., Bertini I., Cremonese G., Da Deppo V., Davidsson B., Debei S., De Cecco M., Fornasier S., Fulle M., Güttler C., Ip W.-H., Kramm J. R., Küppers M., Lara L. M., Lazzarin M., Lopez Moreno J. J., Marzari F., Naletto G., Oklay N., Thomas N., Tubiana C. and Wenzel K.-P. (2016) The global shape, density and rotation of Comet 67P/Churyumov-Gerasimenko from preperihelion Rosetta/OSIRIS observations. *Icarus* **277**, 257–278.

Jourdan F., Andreoli M. A. G., McDonald I. and Maier W. D. (2010) $^{40}Ar/^{39}Ar$ thermochronology of the fossil LL6-chondrite from the Morokweng crater, South Africa. *Geochim. Cosmochim. Acta* **74**, 1734–1747.

Jutzi M., Michel P., Hiraoka K., Nakamura A. M. and Benz W. (2009) Numerical simulations of impacts involving porous bodies II. Comparison with laboratory experiments. *Icarus* **201**, 802–813.

Kagi H. and Fukura S. (2008) Infrared and Raman spectroscopic observations of Central African carbonado and implications for its origin. *Eur. J. Mineral.* **20**, 387–393.

Kimura H., Mann I. and Jessberger E. K. (2003) Composition, structure, and size distribution of dust in the local interstellar cloud. *Astrophys. J.* **583**, 314–321.

Kimura M., Grossman J. N. and Weissberg M. K. (2011) Fe-Ni metal and sulfide minerals in CM chondrites: An indicator for thermal history. *Meteorit. Planet Sci.* **46**, 431–442.

Koeberl C., Masaitis V. L., Shafranovsky G. I., Gilmour I., Langenhorst F. and Schrauder M. (1997) Diamonds from the Popigai impact structure, Russia. *Geology* **25**, 867–970.

Kouketsu Y., Mizukami T., Mori H., Endo S., Aoya M., Hara H., Nakamura D. and Wallis S. (2014) A new approach to develop the Raman carbonaceous material geothermometer for low-grade metamorphism using peak width. *Isl. Arc* **23**, 33–50.

Kramers J. D., Andreoli M. A. G., Atanasova M., Belyanin G. A., Block D., Franklyn C., Harris C., Lekgoathi M., Montross C. S., Ntsoane T., Pischedda V., Segonyane P., Viljoen K. S. and Westraadt J. E. (2013) Unique chemistry of a diamond-bearing pebble from the Libyan Desert Glass strewnfield, SW Egypt: evidence for a shocked comet fragment. *Earth Planet. Sci. Lett.* **382**, 21–31.

Kurat G., Koeberl C., Presper Th., Brandstätter F. and Maurette M. (1994) Petrology and geochemistry of Antarctic micrometeorites. *Geochim. Cosmochim. Acta* **58**, 3879–3904.

Lafuente B., Downs R. T., Yang H. and Stone N. (2015) The power of databases: the RRUFF project. In *Highlights in Mineralogical Crystallography* (eds. T. Armbruster and R. M. Danisi). W. De Gruyter, Berlin, pp. 1–30.

Le Guillou C., Rouzaud J. N., Remusat L., Jambon A. and Bourot-Denise M. (2010) Structures, origin and evolution of various carbon phases in the ureilite Northwest Africa 4742 compared with laboratory-shocked graphite. *Geochim. Cosmochim Acta* **74**, 4167–4185.

Lee J.-Y., Marti K., Severinghaus J. P., Kawamura K., Yoo H.-S., Lee J.-B. and Kim J.-S. (2006) A redetermination of the isotopic abundances of atmospheric Ar. *Geochim. Cosmochim. Acta* **70**, 4507–4512.

Lewis R. S., Amari S. and Anders E. (1994) Interstellar grains in meteorites: II. SiC and its noble gases. *Geochim. Cosmochim. Acta* **58**, 471–494.

Lewis R. S., Srinivasan B. and Anders E. (1975) Host phase of a strange xenon component in Allende. *Science* **190**, 1251–1262.

Magee, Jr., C. W., Teles G., Vicenzi E. P., Taylor W. and Heaney P. (2016) Uranium irradiation history of carbonado diamond; implications for Paleoarchean oxidation in the São Francisco craton. *Geology* **44**, 527–530.

Marty B., Zimmermann L., Burnard P. G., Wieler R., Heber V. S., Burnett D. L., Wiens R. C. and Bochsler P. (2010) Nitrogen isotopes in the recent solar wind from the analysis of Genesis targets: evidence for large scale isotope heterogeneity in the early solar system. *Geochim. Cosmochim. Acta* **74**, 340–355.

Marty B., Chaussidon M., Wiens R. C., Jurewicz A. J. G. and Burnett D. S. (2011) A ^{15}N-poor isotopic composition for the solar system as shown by genesis solar wind samples. *Science* **332**, 1533–1536.

Matsuda J.-I., Fukunaga K. and Ito K. (1991) Noble gas studies in vapor-growth diamonds: comparison with shock-produced diamonds and the origin of diamonds in ureilites. *Geochim. Cosmochim. Acta* **55**, 2011–2023.

Matsuda J. I., Kusumi A., Yajima H. and Syono Y. (1995) Noble gas studies in diamonds synthesized by shock loading in the laboratory and their implications on the origin of diamonds in ureilites. *Geochim. Cosmochim. Acta* **59**, 4939–4949.

McKeegan K., Aléon J., Bradley J., Brownlee D., Busemann H., Butterworth A., Chaussidon M., Fallon S., Floss C., Gilmour J., Gounelle M., Graham G., Guan Y., Heck P. R., Hoppe P., Hutcheon I. D., Huth J., Ishii H., Ito M., Jacobsen S. B., Kearsley A., Leshin L. A., Liu M.-C., Lyon I., Marhas K., Marty B., Matrajt G., Meibom A., Messenger S., Mostefaoui S., Mukhopadhyay S., Nakamura-Messenger K., Nittler L., Palma R., Pepin R. O., Papanastassiou D. A., Robert F., Schlutter D., Snead C. J., Stadermann F. J., Stroud R., Tsou P., Westphal A., Young E. D., Ziegler K., Zimmermann L. and Zinner E. (2006) Isotopic compositions of cometary matter returned by stardust. *Science* **314**, 1724–1728.

Messenger S. (2000) Identification of molecular-cloud material in interplanetary dust particles. *Nature* **404**, 968–971.

Messenger S., Keller L. P., Stadermann F. J., Walker R. M. and Zinner E. (2003) Samples of stars beyond the solar system: silicate grains in interplanetary dust. *Science* **300**, 105–108.

Miyahara M., Ohtani E., El Goresy A., Lin Y., Feng L., Zhang J.-C., Gillet F., Nagase T., Muto J. and Nishijima M. (2015) Unique large diamonds in a ureilite from Almahata Sitta 2008 TC_3 asteroid. *Geochim. Cosmochim. Acta* **163**, 14–26.

Mostefaoui S., Zinner E., Hoppe P., Stadermann F. J. and El Goresy A. (2005) In situ survey of graphite in unequilibrated chondrites: morphologies, C, N, O, and H isotopic ratios. *Meteorit. Planet. Sci.* **40**, 721–743.

Nazarov M. A., Kurat G., Brandstaetter F., Ntaflos T., Chaussidon M. and Hoppe P. (2009) Phosphorus-bearing sulfides and their associations in CM chondrites. *Petrology* **17**, 101–123.

Nguyen, A. N., Busemann, H. and Nittler, L. R. (2007) Remarkably high abundance of presolar grains in interplanetary dust particles collected from the comet Grigg-Skjellerup dust stream. In: Lunar Planetary Science XXXVIII. Lunar Planet. Inst., Houston. #2332(abst.).

Ott U. (2002) Noble gases in meteorites – Trapped components. *Rev. Mineral. Geochem.* **47**, 71–100.

Ozima M., Wieler R., Marty B. and Podosek F. A. (1998) Comparative studies of solar, Q gases and terrestrial noble gases, and implications on the evolution of the solar nebula. *Geochim. Cosmochim. Acta* **62**, 301–314.

Ozima M., Zashu S., Tomura K. and Matsuhisa Y. (1991) Constraints from noble gas contents on the origin of carbonado diamonds. *Nature* **351**, 472–474.

Palme, H. and Jones, A. (2003) Solar system abundances of the elements. In Treatise of Geochemistry, vol. 1. Elsevier, Amsterdam. (ISBN: 0-08-044336-2), pp. 41–61.

Pratesi G., Bindi L. and Cecchi V. M. (2006) Icosahedral coordination of phosphorus in the crystal structure of melliniite, a new phosphide mineral from the Northwest Africa (NWA) 1054 acapulcoite. *Am. Mineral.* **91**, 451–454.

Quirico E., Raynal P.-I. and Bourot-Denise M. (2003) Metamorphic grade of organic matter in six unequilibrated ordinary chondrites. *Meteorit. Planet. Sci* **38**, 795–811.

Quirico E., Borg J., Raynal P.-I., Montagnac G. and D'Hendecourt L. (2005) A micro-Raman survey of 10 IDPs and 6 carbonaceous chondrites. *Planet. Space Sci.* **53**, 1443–1448.

Quirico E., Montagnac G., Rouzaud J.-N., Bonal L., Bourot-Denise M., Duber S. and Reynard B. (2009) Precursor and metamorphic condition effects on Raman spectra of poorly ordered carbonaceous matter in chondrites and coals. *Earth Planet. Sci. Lett.* **287**, 185–193.

Quirico E., Orthous-Daunay F.-R., Beck P., Bonal L., Brunetto R., Dartois E., Pino T., Montagnac G., Rouzaud J.-N., Engrand C. and Duprat J. (2014) Origin of insoluble organic matter in type 1 and 2 chondrites: New clues, new questions. *Geochim. Cosmochim. Acta* **136**, 80–99.

Rai V. K., Murty S. V. S. and Ott U. (2003a) Nitrogen components in ureilites. *Geochim. Cosmochim. Acta* **67**, 2213–2237.

Rai V. K., Murty S. V. S. and Ott U. (2003b) Noble gases in ureilites: cosmogenic, radiogenic, and trapped components. *Geochim. Cosmochim. Acta* **67**, 4435–4456.

Reimold W. U. and Koeberl C. (2014) Impact structures in Africa: a review. *J. Afr. Earth Sci.* **93**, 57–175.

Reich S. and Thomsen C. (2004) Raman spectroscopy of graphite. *Philos. Trans. R. Soc. Lond. A* **362**, 2271–2288.

Romig, Jr., A. D. and Goldstein J. I. (1980) Determination of the Fe-Ni and Fe-Ni-P phase diagrams at low temperatures (700 to 300 °C). *Metall. Trans. A* **11A**, 1151–1159.

Rotundi A., Baratta G. A., Borg J., Brucato J. R., Busemann H., Colangeli L., D'Hendecourt L., Djouadi Z., Ferrini G., Franchi I. A., Fries M., Grossemy F., Keller L. P., Mennella V., Nakamura K., Nittler L. R., Palumbo M. E., Sandford S. A., Steele A. and Wopenka B. (2008) Combined micro-Raman, micro-infrared, and field emission scanning electron microscope analyses of comet 81P/Wild 2 particles collected by Stardust. *Meteorit. Planet. Sci.* **43**, 367–397.

Rubin A. (1997) Igneous graphite in enstatite chondrites. *Min. Mag.* **61**, 699–703.

Salpeter E. E. (1977) Formation and destruction of dust grains. *Ann. Rev. Astron. Astrophys.* **15**, 267–293.

Sandford S. A., Aléon J., Alexander C. M. O'D., Araki T., Bajt S., Baratta G. A., Borg J., Bradley J. P., Brownlee D. E., Brucato J. R., Burchell M. J., Busemann H., Butterworth A., Clemett S. J., Cody G., Colangeli L., Cooper G., D'Hendecourt L., Djouadi Z., Dworkin J. P., Ferrini G., Fleckenstein H., Flynn G. J., Franchi I. A., Fries M., Gilles M. K., Glavin D. P., Gounelle M., Grossemy F., Jacobsen C., Keller L. P., Kilcoyne A. L. D., Leitner J., Matrajt G., Meiborn A., Mennelle V., Mostefaoui S., Nittler L. R., Palumbo M. E., Papanastassiou D. A., Robert F., Rotundi A., Snead C. J., Spencer M. K., Stadermann F. J., Steele A., Stephan T., Tsou P., Tyliszczak T., Westphal A. J., Wirick S., Wopenka B., Yabuta H., Zare R. N. and Zolensky M. E. (2006) Organics captured from comet 81P/Wild 2 by the Stardust spacecraft. *Science* **314**, 1720–1724.

Scott, E. R. D. and Goldstein, J. I. (2012) Occurrence of carbides and graphite in iron meteorites and origin of C-rich irons. In Lunar Planetary Science XLIII. Lunar Planet. Inst., Houston. #2671(abstr.).

Scott E. R. D., Keil K. and Stöffler D. (1992) Shock metamorphism of carbonaceous chondrites. *Geochim. Cosmochim. Acta* **56**, 4281–4293.

Shelkov D., Verchovsky A. B., Milledge H. J. and Pillinger C. T. (1997) Carbonado: a comparison between Brazilian and Ubangui sources with other forms of microcrystalline diamond based on carbon and nitrogen isotopes. *Russ. Geol. Geophys.* **38**, 332–340.

Starkey N. A., Franchi I. A. and Alexander C. M. O'D. (2013) A Raman spectroscopic study of organic matter in interplanetary dust particles and meteorites using multiple wavelength laser excitation. *Meteorit. Planet. Sci.* **48**, 1800–1822.

Thomazo C. and Papineau D. (2013) Biogeochemical cycling of nitrogen on the early earth. *Elements* **9**, 345–351.

Tomeoka K., Yamahana Y. and Sekine T. (1999) Experimental shock metamorphism of the Murchison CM carbonaceous chondrite. *Geochim. Cosmochim. Acta* **63**, 3683–3703.

Trueb L. F. and de Wys E. C. (1969) Carbonado: natural polycrystalline diamond. *Science* **165**, 799–802.

Tschauner O., Ma C., Beckett J. R., Prescher C., Prakapenka V. B. and Rossman G. R. (2014) Discovery of bridgmanite, the most abundant mineral in Earth, in a shocked meteorite. *Science* **346**, 1100–1102.

Urey H. C. (1957) Origin of tektites. *Nature* **179**, 556–557.

Vdovykin G. P. (1973) The Canyon Diablo meteorite. *Space Sci. Rev.* **14**, 758–831.

Virag A., Wopenka B., Amari S., Zinner E., Anders E. and Lewis R. S. (1992) Isotopic, optical, and trace element properties of large single SiC grains from the Murchison meteorite. *Geochim. Cosmochim. Acta* **56**, 1715–1733.

Wasson J. T. (2003) Large aerial bursts; an important class of terrestrial accretionary events. *Astrobiology* **3**, 163–179.

Wooden D. (2002) Comet grains: their IR emission and their relation to ISM grains. *Earth Moon Planets* **89**, 247–287.

Yada, T., Stadermann, F. J., Floss, C., Zinner, E., Nakamura, T., Noguchi, T. and Lea, A. S. (2006) High abundances of presolar silicates in Antarctic micrometeorites; implications for their cometary origins. In Lunar Planetary Science XXXVII. Lunar Planet. Inst., Houston. #1460(abstr.).

Zinner, E., Jadhav, M., Gyngard, F. and Nittler, L.R. (2011) Bonanza, a huge presolar SiC grain of type X. Lunar Planet. Sci. XLII. Lunar Planet. Inst., Houston. #1070(abstr.).

Zolensky M., Barrett R. and Browning L. (1993) Mineralogy and composition of matrix and chondrule rims in carbonaceous chondrites. *Geochim. Cosmochim. Acta* **57**, 3123–3148.

Zolensky M. E. and Thomas K. L. (1995) Iron and iron-nickel sulphides in chondritic interplanetary dust particles. *Geochim. Cosmochim. Acta* **59**, 4707–4712.

Zolensky M. E., Zega T. J., Yano H., Wirick S., Westphal A. J., Mike K., Weisberg M. K., Weber I., Warren J. L., Velbel M. A., Tsuchiyama A., Tsou P., Toppani A., Tomioka N., Tomeoka K., Teslich N., Taheri M., Susini J., Stroud R., Stephan T., Stadermann F. J., Snead C. J., Simon S. B., Simionovici A., See T. H., Robert F., Rietmeijer F. J. M., Rao W., Perronnet M. C., Papanastassiou D. A., Okudaira K., Ohsumi K., Ohnishi I., Nakamura-Messenger K., Nakamura T., Mostefaoui S., Mikouchi T., Meibom A., Matrajt G., Marcus M. A., Leroux H., Lemelle L., Le L., Lanzirotti A., Langenhorst F., Krot A. N., Keller L. P., Kearsley A. T., Joswiak D., Jacob D., Ishii H., Harvey R., Hagiya K., Grossman L., Grossman J. N., Graham G. A., Gounelle M., Gillet P., Genge M. J., Flynn G., Ferroir T., Fallon S., Ebel D. S., Dai Z. R., Cordier P., Clark B., Chi M., Butterworth A. L., Brownlee D. E., Bridges J. C., Brennan S., Brearley A., Bradley J. P., Bleuet P., Bland P. A. and Bastien R. (2006) Mineralogy and petrology of comet 81P/Wild Nucleus samples. *Science* **134**, 1735–1739.

Associate Editor: Eric Quirico